Manuscript submitted to eLife

Quantitative insights into the cyanobacterial cell economy

Tomáš Zavřel[1†*], Marjan Faizi[2†], Cristina Loureiro[3], Gereon Poschmann[4], Kai Stühler[4,5], Maria Sinetova[6], Anna Zorina[6], Ralf Steuer[2*], Jan Červený[1]

***For correspondence:**
zavrel.t@czechglobe.cz (TZ);
ralf.steuer@hu-berlin.de (RS)

[†]These authors contributed equally to this work

[1]Laboratory of Adaptive Biotechnologies, Global Change Research Institute CAS, Brno, Czech Republic; [2]Humboldt-Universität zu Berlin, Institut für Biologie, Fachinstitut für Theoretische Biologie, Berlin, Germany; [3]Department of Applied Physics, Polytechnic University of Valencia, Valencia, Spain; [4]Molecular Proteomics Laboratory, BMFZ, Heinrich-Heine-Universität Düsseldorf, Düsseldorf, Germany; [5]Institute for Molecular Medicine, University Hospital Düsseldorf, Düsseldorf, Germany; [6]Timiryazev Institute of Plant Physiology, Russian Academy of Sciences, Moscow, Russian Federation

Abstract Phototrophic microorganisms are promising resources for green biotechnology. Compared to heterotrophic microorganisms, however, the cellular economy of phototrophic growth is still insufficiently understood. We provide a quantitative analysis of light-limited, light-saturated, and light-inhibited growth of the cyanobacterium *Synechocystis* sp. PCC 6803 using a reproducible cultivation setup. We report key physiological parameters, including growth rate, cell size, and photosynthetic activity over a wide range of light intensities. Intracellular proteins were quantified to monitor proteome allocation as a function of growth rate. Among other physiological adaptations, we identify an upregulation of the translational machinery and downregulation of light harvesting components with increasing light intensity and growth rate. The resulting growth laws are discussed in the context of a coarse-grained model of phototrophic growth and available data obtained by a comprehensive literature search. Our insights into quantitative aspects of cyanobacterial adaptations to different growth rates have implications to understand and optimize photosynthetic productivity.

Introduction

Cyanobacteria are key primary producers in many ecosystems and are an integral part of the global biogeochemical carbon and nitrogen cycles. Due to their fast growth rates, high productivity and amenability to genetic manipulations, cyanobacteria are considered as promising host organisms for synthesis of renewable bioproducts from atmospheric CO_2 (***Al-Haj et al., 2016***; ***Zavřel et al., 2016***), and serve as important model organisms to understand and improve photosynthetic productivity.

Understanding the cellular limits of photosynthetic productivity in cyanobacteria, however, requires quantitative data about cellular physiology and growth: accurate accounting is central to understand the organization, growth and proliferation of cells (***Vázquez-Laslop and Mankin, 2014***). While quantitative insight into the cellular economy of phototrophic microorganisms is still scarce, the cellular economy of heterotrophic growth has been studied extensively—starting with the seminal works of Monod, Neidhardt, and others (***Neidhardt et al., 1990***; ***Neidhardt, 1999***; ***Jun et al., 2018***) to more recent quantitative studies of microbial resource allocation (***Molenaar et al., 2009***; ***Klumpp et al., 2009***; ***Scott et al., 2010***; ***Scott and Hwa, 2011***; ***Bosdriesz et al., 2015***; ***Maitra and Dill, 2015***; ***Weiße et al., 2015***). In response to changing environments, heterotrophic

microorganisms are known to differentially allocate their resources: with increasing growth rate, heterotrophic microorganisms typically exhibit upregulation of ribosomes and other proteins related to translation and protein synthesis (***Scott et al., 2010***; ***Molenaar et al., 2009***; ***Peebo et al., 2015***), exhibit complex changes in transcription profiles, e.g. (***Klumpp et al., 2009***; ***Matsumoto et al., 2013***), and increase cell size (***Kafri et al., 2016***). The molecular limits of heterotrophic growth have been described thoroughly (***Kafri et al., 2016***; ***Erickson et al., 2017***; ***Scott et al., 2014***; ***Metzl-Raz et al., 2017***; ***Klumpp et al., 2013***).

In contrast, only few studies so far have addressed the limits of cyanobacterial growth from an experimental perspective (***Bernstein et al., 2016***; ***Yu et al., 2015***; ***Abernathy et al., 2017***; ***Ungerer et al., 2018***; ***Jahn et al., 2018***). Of particular interest were the adaptations that enable fast photoautotrophic growth (***Bernstein et al., 2016***; ***Yu et al., 2015***; ***Abernathy et al., 2017***; ***Ungerer et al., 2018***). The cyanobacterium with the highest known photoautotrophic growth rate, growing with a doubling time of up to $T_D \sim 1.5$h, is the strain *Synechococcus elongatus* UTEX 2973 (***Ungerer et al., 2018***). Compared to its closest relative, *Synechococcus elongatus* PCC 7942, the strain shows several physiological adaptations, such as higher PSI and cytochrome b_6f content per cell (***Ungerer et al., 2018***), lower metabolite pool in central metabolism, less glycogen accumulation, and higher NADPH concentrations and higher energy charge (relative ATP ratio over ADP and AMP) (***Abernathy et al., 2017***). Recently, a study of the primary transcriptome of *Synechococcus elongatus* UTEX 2973 reported the increased transcription of genes associated with central metabolic pathways, repression of phycobilisome genes, and accelerated glycogen accumulation rates in high light compared to low light conditions (***Tan et al., 2018***).

While these studies point to strain-specific differences and are important for characterizing non-model microbial metabolism (***Abernathy et al., 2017***), the general principles of resource allocation in photoautotrophic metabolism and the laws of phototrophic growth are still poorly understood. Therefore, the aim of this study is to provide a consistent quantitative dataset of cyanobacterial physiology and protein abundance for a range of different light intensities and growth rates—and put the data into the context of published values obtained by a comprehensive literature search as well as into the context of a recent model of photosynthetic resource allocation (***Faizi et al., 2018***). To this end, we chose the widely used model strain *Synechocystis* sp. PCC 6803 (*Synechocystis* hereafter). Since *Synechocystis* exhibits significant variations with respect to both genotype (***Ikeuchi and Tabata, 2001***) and phenotype (***Morris et al., 2016***; ***Zavřel et al., 2017***), we chose the substrain GT-L, a strain that has a documented stable phenotype for at least four years preceding this study. All data are obtained under highly reproducible and controlled experimental conditions, using flat-panel photobioreactors (***Nedbal et al., 2008***) within an identical setup as in the previous studies (***Zavřel et al., 2015b***).

The data obtained in this work provide a resource for quantitative insight into the allocation of cellular components during light-limited, light-saturated, and photoinhibited growth. In dependence of the light intensity and growth rate, we monitor key physiological properties, such as changes in cell size, dry weight, gas exchange (both CO_2 and O_2), as well as changes in abundance of pigments, DNA, total protein, and glycogen. Using proteomics, we show that $\sim 57\%$ (779 out of 1356 identified proteins) proteins changed their abundance in dependence of growth rate, whereas the rest was independent of growth rate. A detailed analysis of changes in individual protein fractions revealed phototrophic "growth laws": abundances of proteins associated with light harvesting decreased with increasing light intensity and growth rate, whereas abundances of proteins associated with translation and biosynthesis increased with increasing light intensity and growth rate—which is in good agreement with recent computational models of cyanobacterial resource allocation (***Burnap, 2015***; ***Rügen et al., 2015***; ***Mueller et al., 2017***; ***Reimers et al., 2017***; ***Faizi et al., 2018***).

Results

Establishing a controlled and reproducible cultivation setup

The *Synechocystis* substrain GT-L (***Zavřel et al., 2015b***) was cultivated in flat panel photobioreactors (Figure 1A) using at least 5 independent reactors in a quasi-continuous (turbidostat) regime (Figure 1B), with red light intensities of $27.5-1100$ µmol(photons) $m^{-2}s^{-1}$, supplemented with a blue light intensity of 27.5 µmol(photons) $m^{-2}s^{-1}$. The addition of blue light avoids possible growth limitations in the absence of short wavelength photons (***Golden, 1995***). Steady-state specific growth rates in turbidostat mode were calculated from monitoring the optical density measured at a wavelength of 680 nm (OD_{680}) as well as from the rate of depletion of spare cultivation medium (as measured by top loading balances). Both methods resulted in similar average values (Figure 1C). Estimation of the specific growth rates based on the medium depletion, however, exhibited higher variance. For further analysis, therefore, only values obtained from the OD_{680} signal are reported.

The measured specific growth rates increased from $\mu = 0.025 \pm 0.002$ h^{-1} to $\mu = 0.104 \pm 0.009$ h^{-1} (corresponding to doubling times of $T_D \approx 27.7\text{h} - 6.9\text{h}$) with increasing light intensities up to 660 µmol(photons) $m^{-2}s^{-1}$ of red light. For higher light intensities the cultures exhibited photoinhibition—a reduction of the specific growth rate induced by high light intensities. Under the highest intensity of 1100 µmol(photons) $m^{-2}s^{-1}$, the specific growth rate decreased to $\mu = 0.093 \pm 0.011$ h^{-1}, corresponding to a doubling time of $T_D = 7.5$ h (Figure 1C-D). The growth curve is consistent with previous measurements of cyanobacterial growth (***Zavřel et al., 2015b***; ***Cordara et al., 2018***) and can be subdivided into three phases: light-limited, light-saturated, and photoinhibited growth.

The cultivation conditions, with (red) light intensity as the only variable, were highly controlled and reproducible. Temperature (32°C) and CO_2 concentration in the sparging gas (0.5%) were set to saturate *Synechocystis* growth in the exponential phase ($OD_{680} = 0.60 - 0.66$), as established in a previous study (***Zavřel et al., 2015b***). Refilling rate of selected nutrients (including Na, N, S, Ca, Mg, P and Fe) during the turbidostat cultivation was sufficient to prevent potential growth limitation by lack of any of these nutrients: see Figure 1 - Figure supplement 1 for further details (the elemental composition of *Synechocystis* cells considered for the calculations was based on data available in the literature).

The experimental setup, including the photobioreactor setup, light quality and intensity, temperature, composition of cultivation medium, CO_2 concentration in the sparging gas, bubbling and stirring rate was identical to the setup used in previous studies for this substrain (***Zavřel et al., 2015b***, ***2017***). We therefore could evaluate the stability of the *Synechocystis* sp. PCC 6803 GT-L phenotype throughout a four year period (2013 - 2017). Figure 1D and 1E show a comparison of the specific growth rates, as well as photosynthetic and respiration rates, from several previous studies (***Zavřel et al., 2015b***, ***2017***) and as yet unpublished data.

Photosynthesis and respiration increase with light intensity and growth rate

The cultivation setup included a probe to monitor dissolved oxygen (dO_2) in the cultivation medium and a gas analyzing unit to measure CO_2 in the gas efflux. Online measurements of gas exchange rates allowed to assess dark respiration rates (measured as O_2 uptake rate during a 5 minutes dark period, see Materials and Methods for further details) as well as photosynthetic activity (gross O_2 release rate and net CO_2 uptake rate). Both photosynthetic activity and dark respiration rates increased with increasing light intensity (Figure 1E, Figure 2C-F).

Between a light intensity of 27.5 and 880 µmol(photons) $m^{-2}s^{-1}$, the gross photosynthetic activity (O_2 release) increased from 30.5 ± 5.7 µmol(O_2) mmol $(Chl)^{-1}$ s^{-1} to 251.6 ± 49.4 µmol(O_2) mmol $(Chl)^{-1}$ s^{-1} , and the dark respiration rate increased from 5.5 ± 2.7 µmol(O_2) mmol $(Chl)^{-1}$ s^{-1} to 40.9 ± 14.6 µmol(O_2) mmol $(Chl)^{-1}$ s^{-1} (Figure 1E).

Of particular interest were changes in gas exchange as a function of the specific growth rate. Figure 2C-D show gas exchange rates as a function of the specific growth rate per gram cellular dry weight (gDW), as well as per cell. Relative to gDW, O_2 release increased from 1.96 ± 0.69 mmol (O_2)

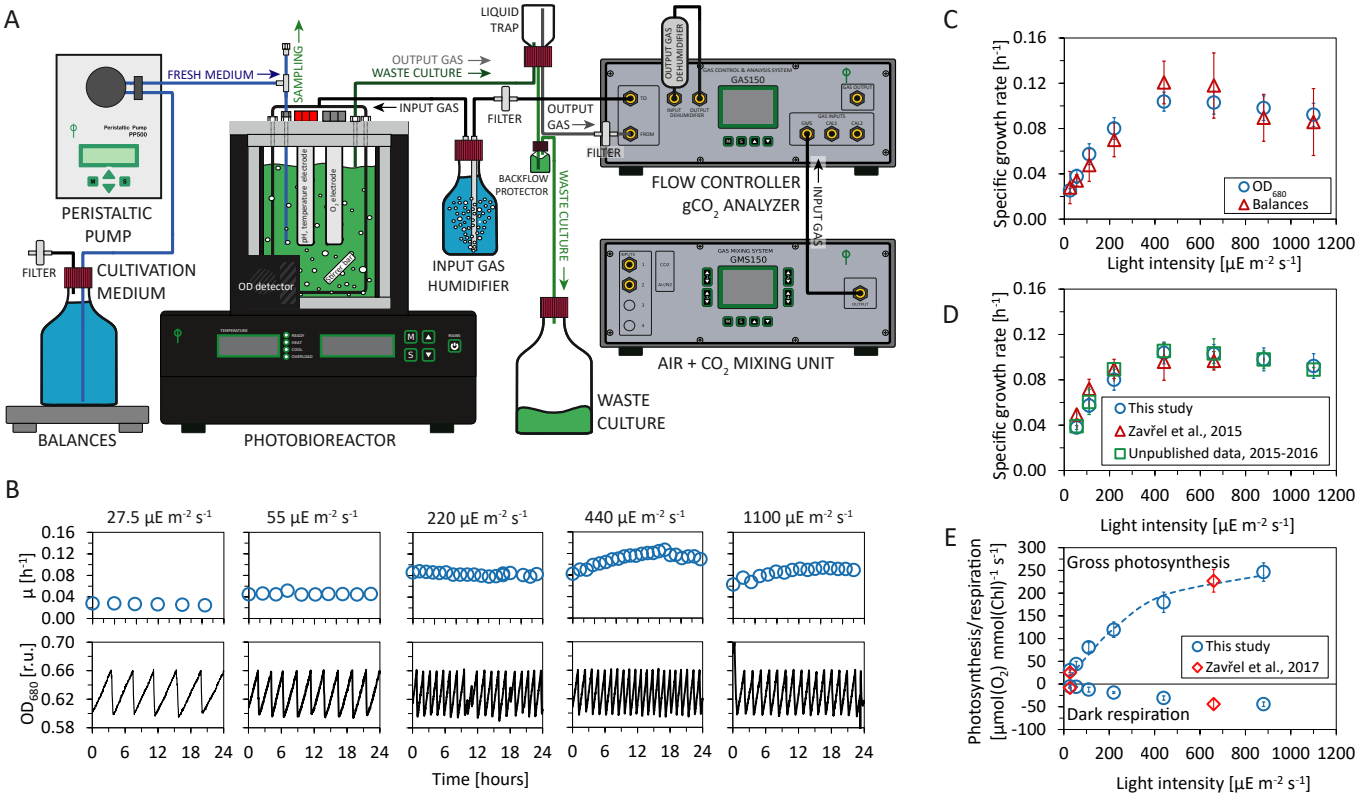

Figure 1. Experimental setup and evaluation of *Synechocystis* sp. PCC 6803 (substrain GT-L) phenotype stability. Panel A: Photobioreactor setup. Cultures were cultivated in a flat-panel photobioreactor vessel (400 mL) in a turbidostat regime according to ***Zavřel et al.*** (***2015b***). Dilution of actively growing culture was based on measurements of optical density at 680 nm (OD_{680}). Inflow air and CO_2 were mixed in a gas mixing unit, the sparging gas flow rate was controlled by a gas analyzing unit. Sparging gas was moistened in a humidifier and, after bubbling through the photobioreactor vessel, separated from the waste culture via a liquid trap. CO_2 concentration in the output gas was measured by an infrared sensor according to ***Červený et al.*** (***2009***). All other parameters were set as described in ***Nedbal et al.*** (***2008***) and ***Červený et al.*** (***2009***). Panel B: Representative measurement of the OD_{680} signal (black lines) within a turbidostat cultivation under increasing red light intensity (supplemented with low intensity of blue light). Calculation of specific growth rates (blue circles) is detailed in Materials and Methods. Panel C: Calculation of growth rates from the OD_{680} signal and from top loading balances that monitored depletion rate of a spare cultivation medium (source data are available in Figure 1 - Source data 1). Panel D: Comparison of specific growth rates using an identical experimental setup throughout four successive years 2013 - 2017 (source data are available in Figure 1 - Source data 2). Panel E: Rates of gross photosynthesis and dark respiration, measured as O_2 evolution and consumption rates directly within the photobioreactor vessel throughout 5 min of light and dark periods in 2016 - 2017 (this study) and in 2015 - 2017 (***Zavřel et al., 2017***). The dashed line represents a P-I curve fit of data from this study according to ***Platt T. , Gallegos C.L., Harrison W.G.*** (***1980***). Source data are available in Figure 1 - Source data 3. Figure 1C: n = 6 - 11, Figure 1D: n = 3 - 11, Figure 1E: n = 4 - 6. Error bars (Figure 1C-1E) represent standard deviations.

Figure 1–Figure supplement 1. Uptake and refilling rates of selected nutrients during the quasi-continuous cultivation.

Figure 1–source data 1. Source data for Figure 1C.

Figure 1–source data 2. Source data for Figure 1D.

Figure 1–source data 3. Source data for Figure 1E.

gDW^{-1} h^{-1} to 5.92 ± 1.26 mmol (O_2) gDW^{-1} h^{-1} for an increase of growth rate from $\mu = 0.025 \pm 0.002$ h^{-1} to $\mu = 0.099 \pm 0.013$ (Figure 2C). Dark respiration rate (O_2 consumption) increased from 0.35 ± 0.12 mmol (O_2) gDW^{-1} h^{-1} to 0.96 ± 0.21 mmol (O_2) gDW^{-1} h^{-1} (Figure 2E-F). Net CO_2 uptake rate increased from 0.78 ± 0.37 mmol (CO_2) gDW^{-1} h^{-1} to 4.01 ± 0.50 mmol (CO_2) gDW^{-1} h^{-1} (Figure 2E).

The measured gas exchange rates correspond to a photosynthesis:respiration (P:R) ratio (gross O_2 release relative to consumption) between 5.6 ± 3.0 and 7.5 ± 2.5. The photosynthetic quotient PQ (net O_2 release:CO_2 fixation) ranged from PQ = 2.1 ± 0.5 to PQ = 1.1 ± 0.4. The changes of both parameters (P:R and PQ) with respect to growth rate were not statistically significant (Kruskal-Wallis test: P:R ratio: $p - value = 0.88$, PQ: $p - value = 0.12$).

Cell morphology and composition acclimate to changes in light intensity and growth rate

Culture samples were harvested under different light intensities to investigate the allocation of key cellular components as a function of growth rate. Cellular parameters included cell count, cell size, cell dry mass, as well as concentrations of glycogen, total protein, total DNA, phycocyanin, allophycocyanin, chlorophyll *a*, and carotenoids. The results (data normalized per gDW as well as per cell) are summarized in Figure 2 as a function of the specific growth rate, the results as a function of light intensity are summarized in Figure 2 - Figure supplement 1.

With increasing growth rate, the volume and weight of *Synechocystis* cells increased (Figure 2A-B). The cell diameter increased from 1.96 ± 0.03 µm to 2.19 ± 0.03 µm, and slightly decreased again under photoinhibition. Since *Synechocystis* has a spherical cell shape, the estimated diameters correspond to cell volumes ranging from 3.97 µm^3 to 5.49 µm^3 (Figure 2A). Changes in cell volume were reflected in changes in cellular dry weight. Dry weight per cell increased from 5.3 ± 1.7 pg cell^{-1} for the slowest specific growth rate to 11.3 ± 2.3 pg cell^{-1} at the maximal growth rate. Under photoinhibition, cellular dry weight again decreased to 8.6 ± 2.6 pg cell^{-1} (Figure 2B, Figure 2 - Figure supplement 1). The ratio of cellular dry weight to cell volume showed no significant change for different growth rates (Kruskal-Wallis test: $p - value = 0.077$).

The amount of glycogen per gDW increased with increasing growth rate, from 84 ± 28 mg gDW^{-1} to 199 ± 35 mg gDW^{-1} for the maximal growth rate, and further increased to 229 ± 72 mg gDW^{-1} under conditions of photoinhibition (Figure 2G). These values correspond to an increase of glycogen per cell from 440 ± 79 fg cell^{-1} to 2329 ± 504 fg cell^{-1} (Figure 2H).

In contrast, the protein content per gDW decreased with increasing growth rate. Protein content per cell, however, did not change significantly for different light intensities and growth rates (Kruskal-Wallis test: $p - value = 0.076$). The absolute values of protein content were between 402 ± 144 and 227 ± 6 mg gDW^{-1} (Figure 2I), and between 2144 ± 482 and 2937 ± 466 fg cell^{-1} (Figure 2J).

Changes in DNA content were only estimated in relative units and are reported relative to the DNA content at the lowest growth rate. With increasing growth rate, the DNA content normalized per gDW decreased to $51 \pm 11\%$ of the initial value (Figure 2I). The (relative) DNA content per cell, however, increased with increasing growth rate up to $137 \pm 19\%$ of its initial value. Under conditions of photoinhibition, the relative DNA content per cell decreased again to $94 \pm 29\%$ of the initial value (Figure 2J).

Relative to gDW, the amounts of phycobiliproteins, chlorophyll *a* and carotenoids decreased with increasing growth rate. Under conditions of photoinhibition, we observed additional reduction of these pigments per gDW (Figure 2K,M). When considering the concentrations per cell, however, the respective amounts initially increased with increasing growth rates, and decreased again under conditions of photoinhibition. Overall, pigment content decreased with increasing light intensity (irrespective of normalization), with the exception of carotenoids which exhibited a slight increase per cell as a function of light intensity. The changes of pigment amounts as a function of growth rate (relative to gDW as well as per cell) were significant (Kruskal-Wallis test: $p - value < 0.05$, see Materials and Methods for further details). The absolute amounts of phycocyanin were between 86.4 ± 30.7 and 26.5 ± 7.5 mg gDW^{-1}, corresponding to 172 ± 29 and 620 ± 63 fg cell^{-1} (Figure 2K,L),

the amounts of allophycocyanin were between 14.8 ± 5.3 and 6.7 ± 1.9 mg gDW^{-1}, corresponding to 57 ± 10 and 123 ± 15 fg cell^{-1} (Figure 2K,L). The absolute amounts of chlorophyll a were between 16 ± 5.2 and 5.8 ± 1.6 mg gDW^{-1}, corresponding to a range between 50 ± 10 and 96 ± 14 fg cell^{-1} (Figure 2M,N), the absolute amounts of carotenoids were between 4.4 ± 0.7 and 2.6 ± 0.5 mg gDW^{-1}, corresponding to a range between 22 ± 3 and 29 ± 6 fg cell^{-1} (Figure 2M,N).

To put the data into context, we conducted a comprehensive literature research with respect to reported physiological parameters of *Synechocystis* sp. PCC 6803. The results are summarized in Figure 2 - Figure supplement 2, and the data include also meta information on experimental conditions. Overall, the values obtained in this study are in good agreement with the previously reported values. Individual parameters, however, exhibit high variability due to the wide range of different experimental conditions.

Proteome allocation as a function of growth rate

Culture samples for 6 light intensities were harvested to obtain quantitative proteome profiles using mass spectrometry, with 5 biological replicates for each light intensity. We chose a label-free quantification (LFQ) approach to access relative and absolute protein amounts. Here, the peptide precursor ion intensities (MS1) were used for protein quantification. The results of the proteomics analysis are summarized in Figure 3. We identified 1356 proteins (the complete list is provided in Figure 3 - Source data 1). Of these, the (relative) abundances of 779 proteins (57%) significantly changed with growth rate (Kruskal-Wallis test: $p - value < 0.05$), the (relative) abundances of the remaining 577 proteins (43%) were independent of growth rate. We obtained functional annotation for all 1356 proteins using the Gene Ontology (GO) database (***Ashburner et al., 2000***). Of the 779 growth-dependent proteins, 450 were annotated with non-trivial categories (excluding categories such as *unknown* or *putative*), of the 577 growth-independent proteins, 303 were annotated with non-trivial categories. To facilitate the analysis, the functional annotation was mapped to a subset GO slim (higher level GO terms, ***Klopfenstein et al.*** (***2018***)), which resulted in 40 distinct GO terms (each protein might be associated with more than one annotation). Significant differences (Fisher's exact test, $p - value < 0.05$) between growth-dependent and growth-independent annotations are summarized in Table 1. Growth-dependent proteins exhibited an over-representation of categories such as *Translation*, *Protein folding*, *Cell division* and *Photosynthesis*, among others.

To allow for a more detailed analysis of growth-dependent proteins, the changes in abundance of the 779 proteins were grouped into 7 clusters using k-means clustering (Figure 3 - Figure supplement 3). The number of clusters was determined using the elbow method. The identified clusters corresponded either to upregulation (cluster 1 and 6), or downregulation of protein abundance with growth rate (cluster 2, 5, 7) or more complex changes (cluster 3 and 4). The results of the clustering analysis are summarized in Figure 3, along with an annotation matrix that highlights the prevalent function (GO slim) categories for each cluster. The growth-dependent proteins encompass 37 distinct annotations mapped to GO slim categories.

Cluster 1 (192 proteins) and 6 (41 proteins) exhibit increasing abundance for increasing light intensity and growth rate. Prevalent annotations are *biosynthetic processes*, such as *cellular nitrogen compound metabolic processes*, *cellular amino acid metabolic processes*, as well as, for cluster 1, *translation*. Cluster with low variation (Cluster 2, 218 proteins) and cluster with ambiguous shapes (cluster 4, 124 proteins) exhibit a similar set of categories as cluster 1 and 6. In contrast, both clusters that exhibit a clear decrease with increasing light intensity and growth rate (cluster 5, 65 proteins and cluster 7, 79 proteins) are both annotated with *photosynthesis* as the highest-ranking annotation. Finally, cluster 3 (2 proteins) exhibits a sharp upregulation during photoinhibition, with both proteins annotated with the categories *transport* and *transmembrane processes*.

We note that, similar to some of the physiological properties as shown in Figure 2, the abundances of clusters 1, 3, 4, 6 and 7 exhibited a characteristic "kink" at high growth rates corresponding to a sharp up- or downregulation under photoinhibition.

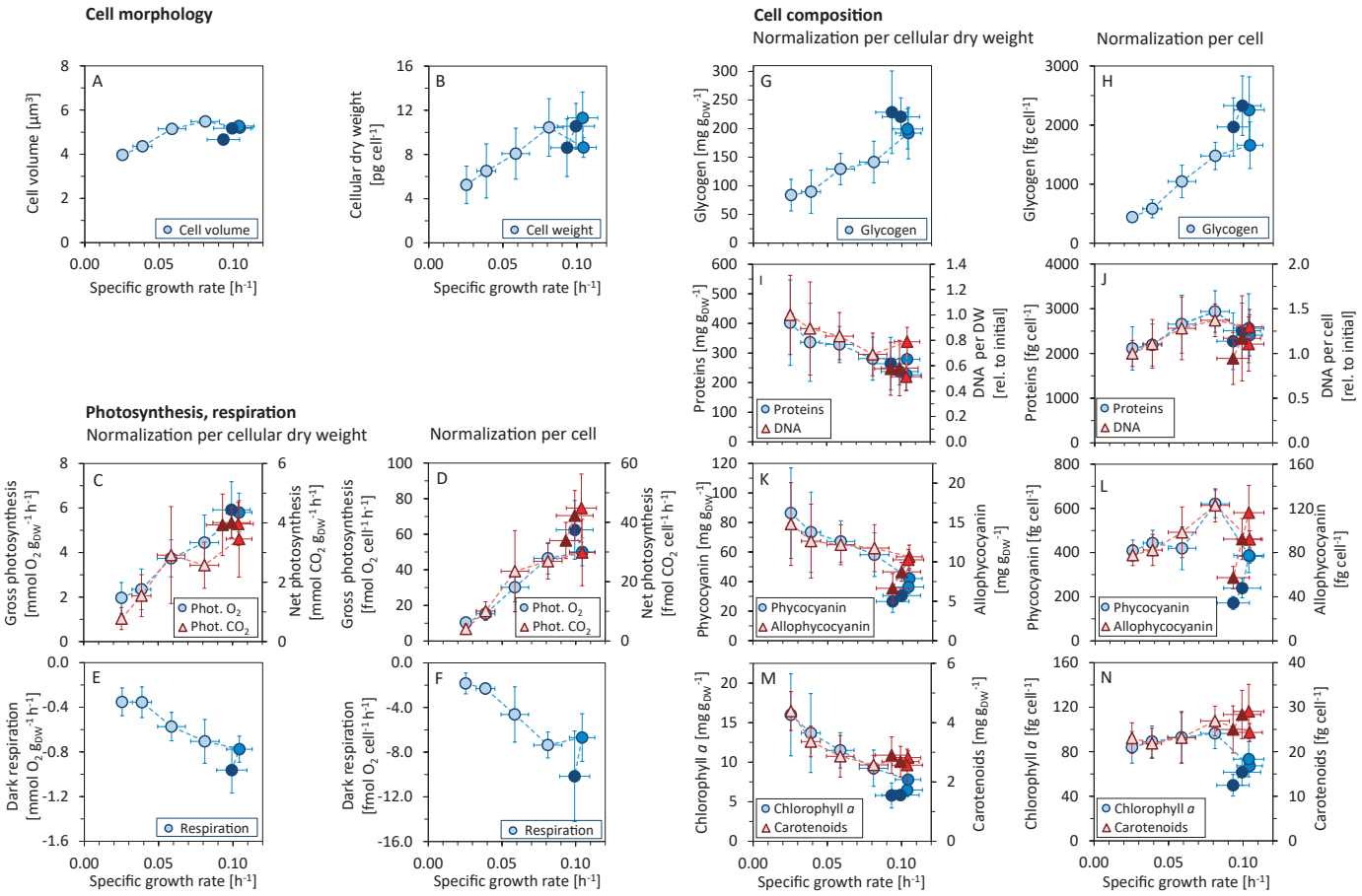

Figure 2. Variations in morphology and composition of *Synechocystis* cells with changing growth rate. Under increasing light intensity and changing growth rate, the following parameters were estimated: cellular volume (A) and dry weight (B), gross photosynthesis (C, D) and dark respiration (E, F), and content of glycogen (G, H), proteins, DNA (I, J), phycobiliproteins (K, L), chlorophyll *a* and carotenoids (M, N). The data are plotted relative to cellular dry weight (C, E, G, I, K, M) as well as per cell (D, F, H, J, L, N). DNA content was normalized to its initial value after standardization per dry weight and per cell, the measurement was only semi-quantitative. All values represent averages from 3 – 11 independent biological replicates, error bars represent standard deviations. If error bars are not visible (panel A), the standard deviation was too small for visualization. Within each figure, data points are displayed in three different color shades to reflect (from bright to dark) light-limited, light-saturated and light-inhibited growth. Data plotted as a function of light intensity are available in Figure 2 - Figure supplement 1. Comparison with data available in the literature is summarized in Figure 2 - Figure supplement 2.

Figure 2–Figure supplement 1. Allocation of key cellular resources as a function of light intensity

Figure 2–Figure supplement 2. Comparison of the values measured in this study with data reported in the literature.

Figure 2–source data 1. Source data for Figure 2.

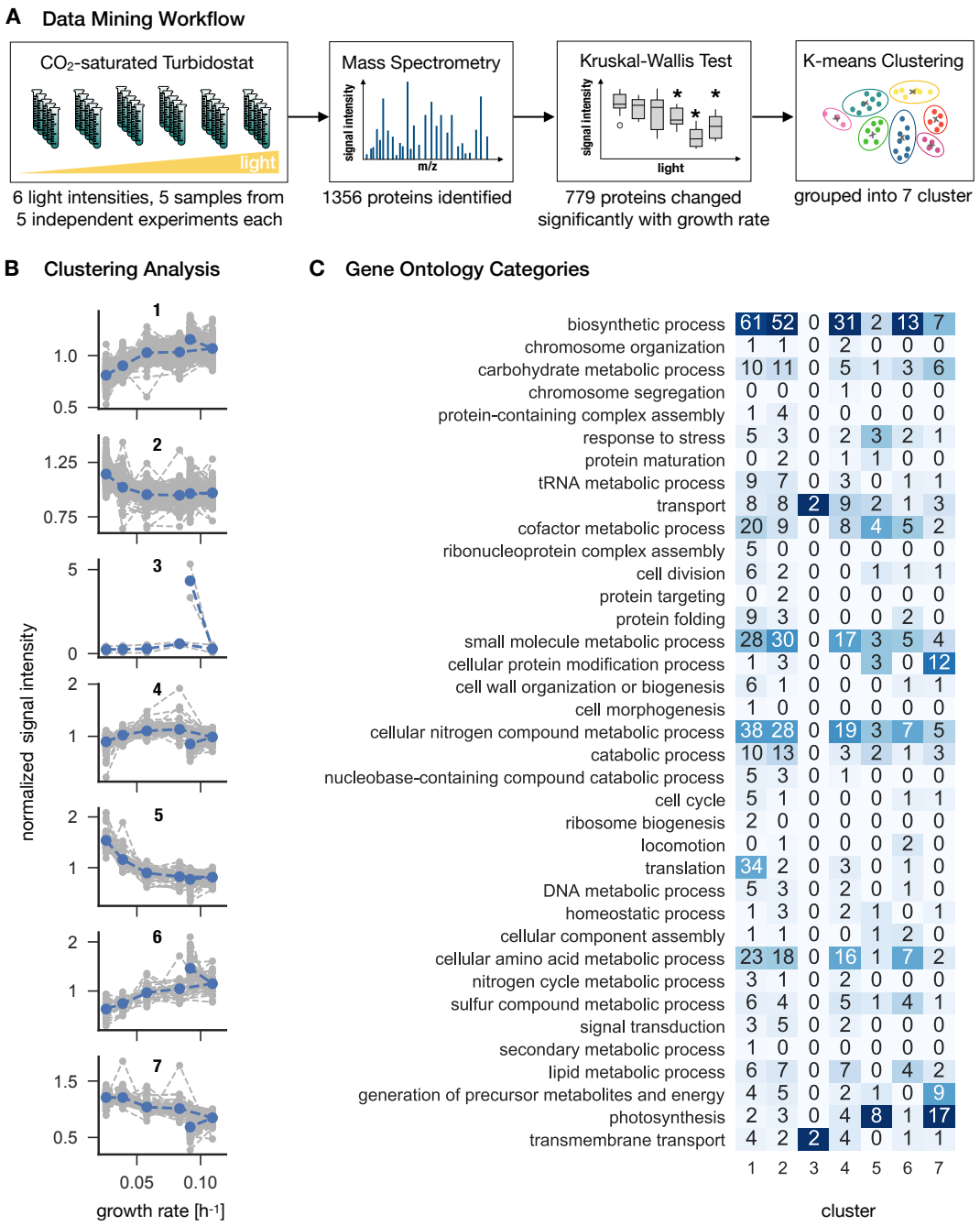

Figure 3. *Synechocystis* proteome allocation as a function of growth rate. Panel A: The workflow. Samples were harvested and analyzed by mass spectrometry (the proteomics dataset is available in Figure 3 - Source data 1). A Kruskal-Wallis test was used to distinguish between growth-dependent and growth-independent proteins. 779 growth-dependent and 577 growth-independent proteins were identified. Panel B: Clustering analysis. Based on k-means clustering analysis (Figure 3 - Figure supplement 3), the 779 growth-dependent proteins were separated into 7 clusters. Gray dashed lines represent protein abundances as medians of 5 biological replicates, normalized by the respective means. Blue dashed lines represent centroids of the respective clusters. Panel C: Proteins were annotated using the GO classes, the matrix represents the annotation mapped to GO slim categories. Proteins can be associated to several GO slim categories. The highest ranking annotation per cluster is highlighted in dark blue.

Figure 3–source data 1. Proteomics dataset.

Figure 3–Figure supplement 1. List of growth-dependent proteins.

Figure 3–Figure supplement 2. List of growth-independent proteins.

Figure 3–Figure supplement 3. Elbow method for the identification of an appropriate number of clusters (grey dashed line at 7 clusters).

Table 1. Gene Ontology (GO) slim categories (***Klopfenstein et al., 2018***) with the amount of associated growth-dependent and independent proteins. A complete list of the GO slim categories is provided in Table1-source data 1. Here, only categories that exhibit a significant difference (Fisher's exact test, $p - value < 0.05$) between growth-dependent and independent groups are listed. Shown is the number of annotations per category.

Gene Ontology categories	Growth dependent	Growth independent
Translation	40	13
Transport	36	14
Photosynthesis	36	8
Catabolic process	32	4
Protein folding	14	3
Cell division	12	0
Cell wall organization or biogenesis	10	1
Cell cycle	9	0

Table 1–source data 1. List of all 40 GO slim categories with the respective amounts of growth-dependent and growth-independent proteins (and their cluster associations).

Visualization of functional annotation using proteomaps

To complement the clustering analysis, we used the proteomaps software (www.proteomaps.net, ***Liebermeister et al.*** (***2014***)) to visualize the relative abundances of the identified proteins for different light conditions. To this end, iBAQ intensities were used as an approximation for quantitative protein amounts. Here, the measured precursor ion intensities (MS1) for each individual protein are summed up and divided by the number of theoretically observable peptides for the respective protein. The number of theoretically observable peptides is calculated for each protein by an in silico digestion of the respective database sequence and only peptides between 6 and 30 amino acids in length are considered for the calculations. We emphasize that, while iBAQ intensities are roughly proportional to the molar amounts of the proteins, iBAQ intensities only refer to identified proteins and do not reflect the whole proteome: the sum of all proteins used for the generation of proteomaps is based on identified proteins only, with the unidentified proteins being neglected. Therefore, the proportionality factor could change from sample to sample, and the intensities are interpreted only as approximations that provide insight into the expected overall abundances.

Figure 4 shows proteomaps for three distinct growth regimes: light-limited growth at 27.5 µmol(photons) $m^{-2}s^{-1}$ (specific growth rate $\mu = 0.025$ h^{-1}), light-saturated growth at 440 µmol(photons) $m^{-2}s^{-1}$ (specific growth rate $\mu = 0.104$ h^{-1}), and photoinhibited growth at 1100 µmol(photons) $m^{-2}s^{-1}$ (specific growth rate $\mu = 0.093$ h^{-1}). The full set of proteomaps is available in Figure 4 - Figure supplement 1.

The proteomaps (annotated using Cyanobase (***Fujisawa et al., 2017***) mapped to custom KEGG annotation) show similar trends as the clustering analysis: upregulation of proteins associated with translational processes and ribosomes with increasing light intensity and growth rate, and downregulation of photosynthetic and light harvesting proteins with increasing light intensity and growth rate.

A coarse-grained model provides insight into proteome allocation

To interpret the experimental results on cyanobacterial physiology, we made use of a semi-quantitative resource allocation model of cyanobacterial phototrophic growth. The model was adopted from ***Faizi et al.*** (***2018***) and is summarized in Figure 5. In brief, the model includes coarse-grained proteome fractions for cellular processes related to growth, including carbon uptake T, metabolism M, photosynthesis P, and ribosomes R. The model describes light-dependent cyanobacterial growth at saturating conditions of external inorganic carbon. Compared to the original model from ***Faizi et al.*** (***2018***), we now include a growth-independent protein fraction Q

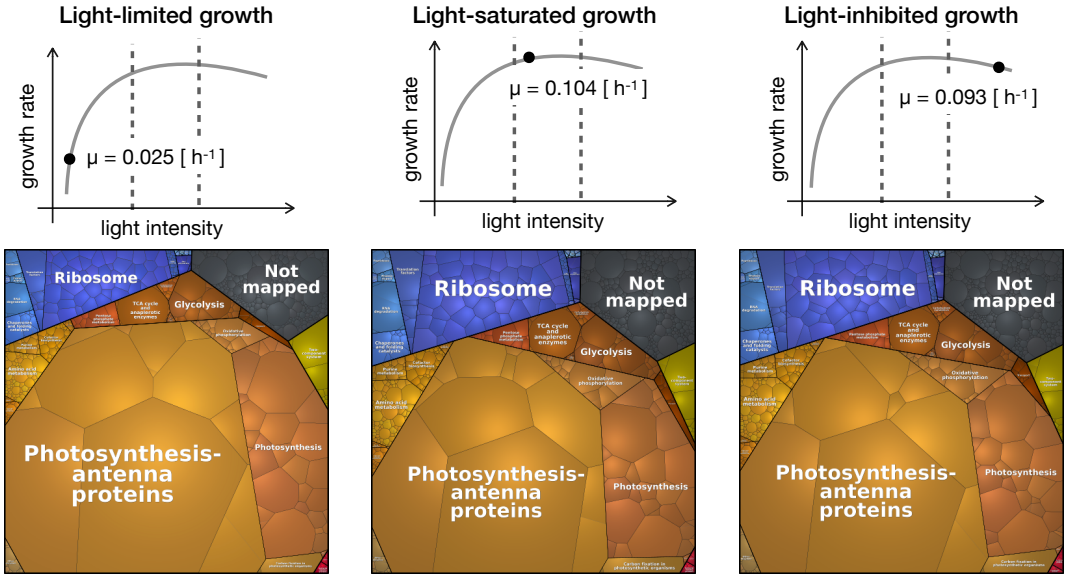

Figure 4. Proteomaps of proteome reallocation in *Synechocystis* under light-limited (27.5 µmol(photons) $m^{-2}s^{-1}$), light-saturated (440 µmol(photons) $m^{-2}s^{-1}$) and photoinhibited growth (1100 µmol(photons) $m^{-2}s^{-1}$). Each tile represents a single protein. The tiles are arranged and coloured according to Cyanobase annotation such that larger regions correspond to the functional categories. The tile sizes represent relative protein abundances. The proteomaps were generated using the platform available at http://bionic-vis.biologie.uni-greifswald.de/ (Version 1, ***Liebermeister et al.*** (***2014***)). Proteomaps of levels 2, 3 and 4 (that correspond to two successive levels of functional categories and to the level of individual proteins) from 6 light conditions are available in Figure 4 - supplement 1.

Figure 4–Figure supplement 1. Proteomaps of levels 2, 3 and 4.

that accounts for half of the proteome mass. All further (minor) modifications and changes in the model definition are detailed in Materials and Methods.

Following ***Faizi et al.*** (***2018***), all kinetic parameters were sourced from the primary literature, except the parameters for the photosynthetic cross section, photosynthetic turnover rate, and the rate constant for photoinhibition (see Materials and Methods for further details). These 3 parameters were fitted numerically, such that the predicted maximal growth rate μ (Figure 1C-D) matched the experimental values (Figure 5B). The stoichiometry and energy requirements for biosynthesis were approximated using a genome-scale model (***Knoop et al., 2013***). No proteomics data were used during model parametrization and fitting. All parameters and model definitions are provided in Figure 5 - Figure supplement 1.

Evaluation of the model is based on the assumption of (evolutionary) optimality. That is, the model is solved using an optimization algorithm that maximizes the specific growth rate μ as a function of protein allocation. In this way, the model is able to predict how the coarse-grained proteome fractions are optimally allocated with increasing light intensity (Figure 5B). These predictions provide a reference to which the experimental data can be compared. We emphasize that such a comparison does not presuppose that proteome allocation in *Synechocystis* is necessarily optimal.

The model predictions are shown in Figure 6, together with data from the experimental analysis. The protein fraction associated with biosynthesis (M), as well as the ribosomal fraction (R), increase-with increasing growth rate—in accordance with known growth laws of heterotrophic growth (***Scott et al., 2010***; ***Weiße et al., 2015***). In contrast, the protein fraction associated with photosynthesis (P, light harvesting and photosystems) decreases with increasing light intensity and growth rate. We highlight that the predicted growth laws exhibit a characteristic 'kink' under conditions of photoinhibition—a feature that is different from all reported growth laws for heterotrophic growth.

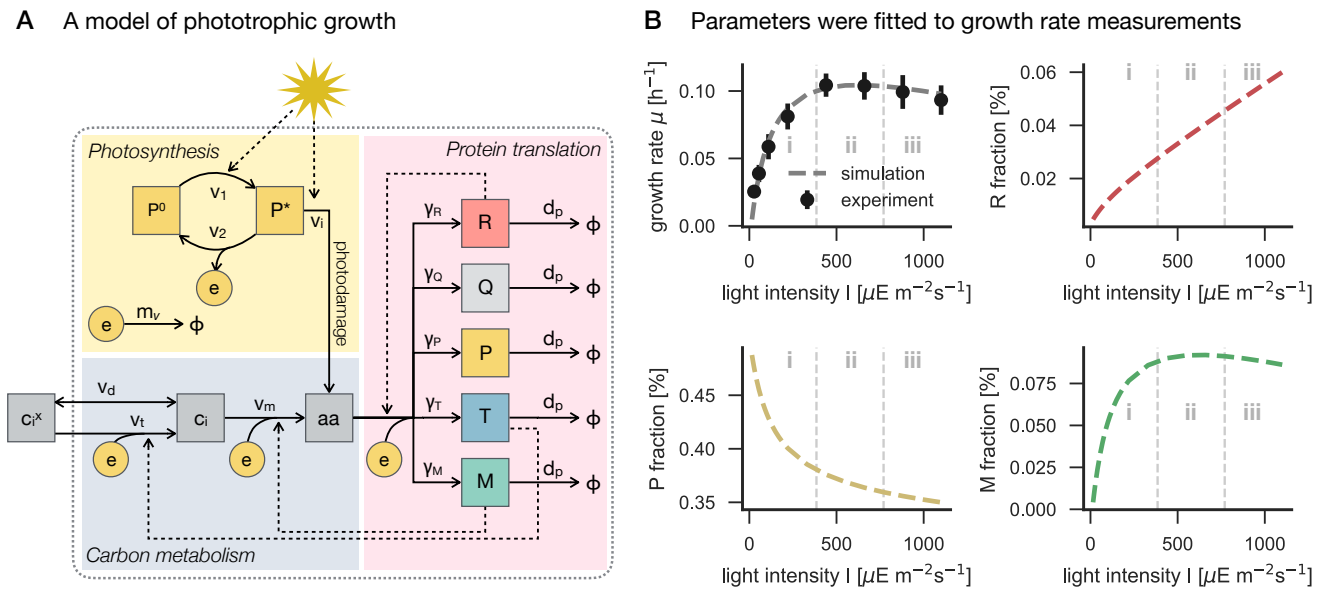

Figure 5. Panel A: A coarse-grained model of phototrophic growth, adopted from ***Faizi et al. (2018)***. The model describes optimal proteome allocation under conditions of (i) light-limited, (ii) light-saturated and (iii) light-inhibited growth. Coarse-grained cellular processes include passive (v_d) and active import (v_t) of external inorganic carbon c_i^x, conversion of inorganic carbon c_i into amino acids aa (v_m), light harvesting and provision of cellular energy by photosynthesis (v_1 and v_2), as well as maintenance and photodamage (m_v and v_i). Amino acids are translated into coarse-grained protein fractions for transport (T), metabolism (M), ribosomes (R), photosynthetic electron transport (P), as well as a growth-independent proteome fraction Q. Translation is limited by the amount of available ribosomes R. Panel B: The model reproduces the measured growth curve (Figure 1C-D) as a function of light intensity. Shown are the specific growth rate μ, as well as the main proteome fractions, ribosome R, photosynthetic electron transport P, and metabolism M, as a function of light intensity.

Figure 5–Figure supplement 1. Summary of the proteome allocation model.

Testing protein allocation using immunoblotting analysis

In addition to large-scale proteomics, we tested the changes of selected proteins as a function of growth rate using immunoblotting analysis. Specifically, we measured the abundances of PsaC (an essential component of PSI), PsbA (the D1 protein of PSII), the RuBisCO subunit RbcL, and the ribosomal proteins S1 and L1 under increasing growth rate. Additionally, the absolute amounts of PsbA, PsaC, and RbcL proteins were estimated by serial dilution of protein standards (see Materials and Methods for details).

The immunoblotting results are summarized in Figure 6C, together with the model predictions and selected proteomics data. Overall, the trends confirm the results of the previous sections—and correspond to the changes obtained from the protein allocation model. The ribosomal proteins S1 and L1 increased with increasing growth rate, with a characteristic upwards 'kink' under photoinhibition. The relative amount of PsbA, the D1 protein of PSII, decreased with increasing growth rate, with a characteristic downward 'kink' under photoinhibition (albeit less pronounced than for ribosomal proteins). PsaC associated to PSI followed a similar trend but with high variance. In contrast to the overall behavior of proteins associated with metabolism, the RuBisCO subunit RbcL exhibited a (slight) increase for increasing growth rates, in accordance with the model predictions (Figure 6C).

Quantitative evaluation of selected protein complexes

Using the combined data of iBAQ intensities and quantification by immunoblotting and mass spectrometry, allows us to provide estimates of absolute amounts of selected protein complexes in *Synechocystis* cells. The results are summarized in Table 2, details of the calculations are listed in Table 2-Source data 1.

The most abundant proteins in *Synechocystis* cells were proteins associated to photosynthesis

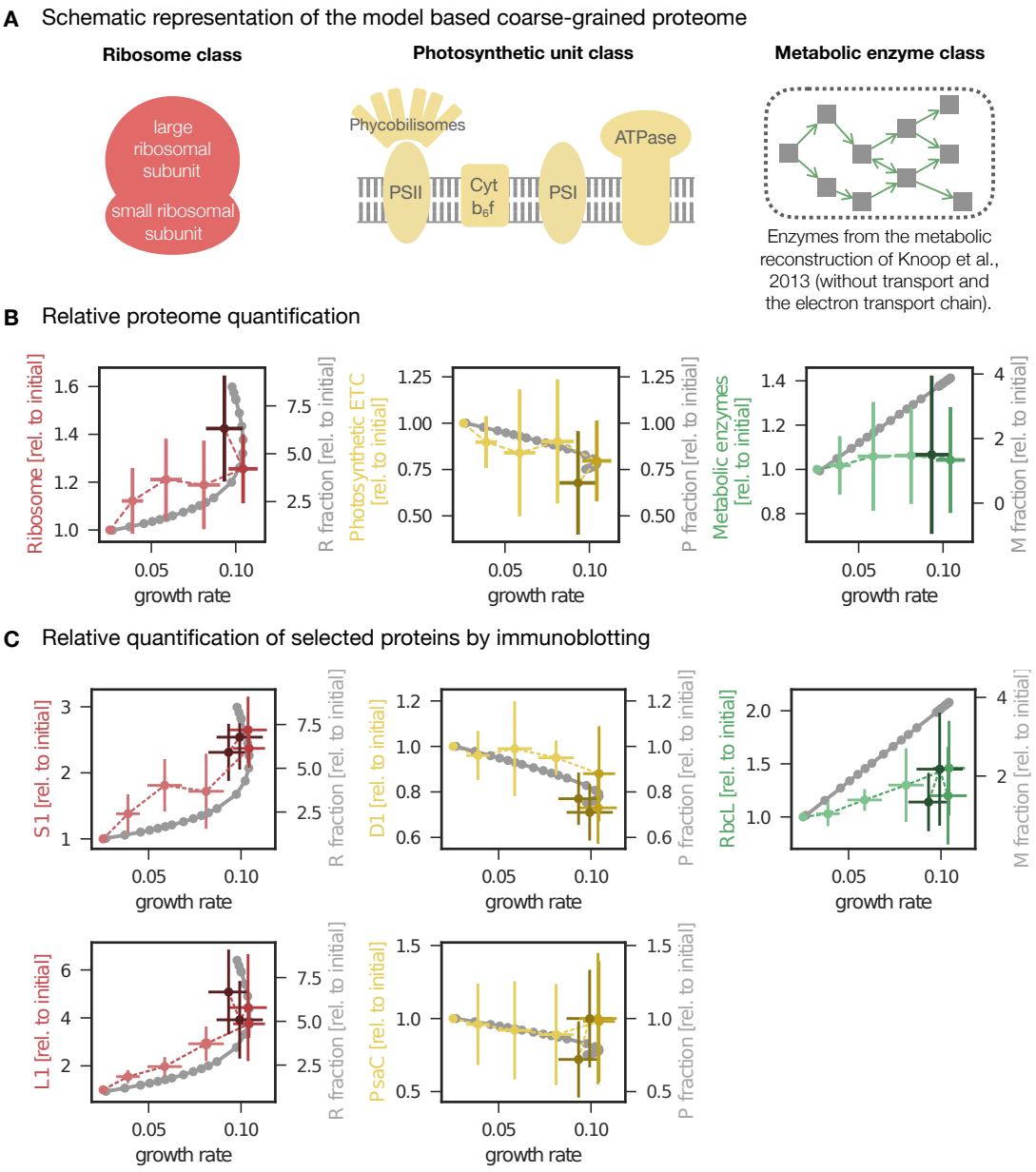

Figure 6. Changes in protein abundance as a function of specific growth rate compared to the predictions obtained from a computational model of proteome allocation. Panel A: Schematic representation of ribosome, photosynthetic units and metabolic enzyme classes considered in the proteome allocation model. Panel B: Relative proteomics data (LFQ, label-free quantification intensities, left axes, mean fold change ± SD) of protein classes in comparison with the model predictions (grey lines, right axes). Panel C: Relative protein abundances obtained by immunoblotting analysis for selected proteins (left axes, median fold change ± SD) in comparison with coarse-grained model predictions (grey lines, right axes). Experimental values represent averages from 5 independent experiments, the error bars represent standard deviations. Panels B-C: The experimental data points are displayed in three different color shading to reflect (from bright to dark) light-limited, light-saturated and light-inhibited growth. The full dataset of the immunoblotting analysis is provided in Figure 6 - Source data 1 and Figure 6 - Figure supplement 1. The list of proteins considered for ribosome, photosynthetic unit and metabolic enzyme classes is listed in Figure 6 - source data 2.

Figure 6–source data 1. Results of the immunoblotting analysis.

Figure 6–source data 2. List of proteins considered for ribosome, photosynthetic unit and metabolic enzyme classes.

Figure 6–Figure supplement 1. Immunoblots and a list of antibodies used for the immunoblotting analysis.

Figure 6–Figure supplement 2. Influence of constant enzyme fractions in the model on cellular growth rate.

Table 2. Quantification of selected protein complexes in *Synechocystis* cells. Protein abundances were estimated as molecules per cell, as inferred from mass spectrometry, immunoblotting and spectrophotometric analysis. The stoichiometries of protein complexes were based on Uniprot (www.uniprot.org, ***UniProt Consortium* (*2018*)**) and RCSB (www.rcsb.org, ***Berman et al.* (*2000*)**) databases. Protein abundances are not precise estimates but indicate ranges. The range in the second column reflects the minimal and maximal protein amounts estimated across all light intensities studied in this work. Estimation of protein abundances is detailed in Table 2-Source data 1, a list of all proteins is provided in Table 2-Source data 2. The experimental conditions of (***Moal and Lagoutte, 2012***) are comparable to the conditions used in this study with the exception of high light used here and distinct *Synechocystis* substrains (Figure 2 - Figure supplement 2).

Protein complex	Molecules per cell	Method	Stoichiometry	Reference
Elongation factor	179000-274000	Proteomics	TufA	This study
Phosphoglycerate kinase	45000 - 73000	Proteomics	Pgk	This study
Ribosome small subunit	36000 - 66000	Proteomics	Rps1A,1B,B,C,D,E,F,G,H,I,J,K,L,M,N,O,P,Q,R,S,T,U	This study
Phycobilisome (phycocyanin)	12000 - 23000	Proteomics	$((CpcA,B)_{18},C1,C2,D,G)_6$	This study
	26000 - 66000	Spectrophotometry		This study
Photosystem I	31000 - 63000	Proteomics	$(PsaA,B,C,D,E,F,I,J,K,L,M,X)_3$	This study
	96000	Spetroscopy		(*Keren et al., 2004*)
	540000	Spetroscopy		(*Moal and Lagoutte, 2012*)
Ribosome large subunit	33000 - 54000	Proteomics	RplA,B,C,D,E,F,I,J,K,L,M,N,O,P,Q,R,S,T,U,V,W,X,Y, RpmA,B,C,E,F,G,H,I,J	This study
Transketolase	31000 - 50000	Proteomics	$TktA_2$	This study
PII signal transducing protein	36000 - 46000	Proteomics	$GlnB_3$	This study
Photosystem II	23000 - 46000	Proteomics	$(PsbA1,A2,B,C,D,E,F,H,I,J,K,L,M,N,O,T,U,V,X,Y,Z, Ycf12)_2$	This study
	17000 - 29000	Immunoblotting		This study
	100000	Spetroscopy		(*Moal and Lagoutte, 2012*)
RuBisCO	26000 - 43000	Proteomics	$(RbcL, RbcS)_8$	This study
	39000 - 63000	Immunoblotting		This study
Ferredoxin-NADP reductase (FNR)	33000 - 42000	Proteomics	PetH	This study
	140000	Immunoblotting		(*Moal and Lagoutte, 2012*)
D-fructose 1,6-bisphosphatase class 2	29000 - 36000	Proteomics	Slr20944	This study
Phycobilisome (allophycocyanin)	19000 - 38000	Proteomics	$(ApcA,B)_{34},C_6,D_2,E_6,F_2$	This study
	9000 - 19000	Spectrophotometry		This study
G3P dehydrogenase	21000 - 32000	Proteomics	$Gap2_4$	This study
Plastocyanin	15000 - 29000	Proteomics	PetE	This study
Superoxide dismutase [Fe]	14000 - 25000	Proteomics	$SodB_2$	This study
Orange carotenoid protein	15000 - 24000	Proteomics	$Slr1963_2$	This study
RNA polymerase	8000 - 15000	Proteomics	$RpoA_2,B,C1,C2,D,E,F$	This study
Cytochrome b6/f	8000 - 15000	Proteomics	$(PetA,B,C2,D,G,L,M,N)_2$	This study
Chaperonine GroEL	7000 - 13000	Proteomics	$GroL1_{14}$	This study
Ribosome recycling factor	6000 - 7000	Proteomics	Frr	This study
Phosphoglycerate dehydrogenase	3000 - 5000	Proteomics	$SerA_4$	This study
Pyruvate dehydrogenase	3000 - 4000	Proteomics	$(PdhA, PdhB)_2$	This study
Glutamine synthetase	2000 - 4000	Proteomics	$GlnA_{12}$	This study
Isocitrate dehydrogenase	2000 - 3000	Proteomics	Icd_2	This study
Glycogen synthase	2000 - 3000	Proteomics	GlgA1	This study
DNA polymerase III	1000 - 2000	Proteomics	$DnaN_2$	This study
Pyruvate kinase	1000 - 2000	Proteomics	$Pyk2_4$	This study
Acetyl-coenzyme A carboxylase	1000	Proteomics	$AccB, AccC, AccA_2,ACCD_2$	This study
Carbonic anhydrase	400 - 700	Proteomics	$IcfA_6$	This study
Acetyl-coenzyme A reductase	300 - 600	Proteomics	$PhaB_4$	This study
Circadian clock proteins KaiA / KaiB / KaiC	200 - 500	Proteomics	$KaiA_2$ / $KaiB_4$ / $KaiC_6$	This study

Table 2–source data 1. Calculations of selected protein complex copies in *Synechocystis* cells.
Table 2–source data 2. List of all proteins quantified by proteomics measurements in *Synechocystis* cells.

and carbon fixation, in particular proteins related to phycobilisomes, photosystems and RuBisCO. Aside from protein complexes, the most abundant monomeric protein was the elongation factor Tu (TufA) with approximately $2 - 3 \cdot 10^5$ copies per cell. Abundances of photosynthetic proteins were generally one to two orders of magnitude lower, similar to ribosomal and other proteins, including phosphoglycerate kinase, transketolase, PII signal transducing protein, ferredoxin-NADP reductase, D-fructose 1,6-bisphosphatase, glyceraldehyde-3-phosphate dehydrogenase, plastocyanin, superoxide dismutase, orange carotenoid protein, RNA polymerase, cytochrome b_6f and chaperonine GroEL.

Table 2 also includes several previous estimates of protein abundances. We note that a direct comparison is challenging due to differences in cultivation conditions, including type of cultivation and cultivation vessel, cultivation media, irradiance, temperature, aeration, pH and the particular *Synechocystis* substrain (see Figure 2 - Figure supplement 2 for further details on particular experimental conditions).

Discussion

Quantitative resource allocation in cyanobacteria

Cyanobacteria are increasingly important host organisms for green biotechnology, but as yet insight

into resource allocation of these organisms is restricted to few studies (***Abernathy et al., 2017***; ***Burnap, 2015***; ***Faizi et al., 2018***; ***Jahn et al., 2018***). The scarcity of data is partially due to the fact that a quantitative experimental assessment of phototrophic growth is subject to a number of technical difficulties and standardized cultivation conditions are not available. The diversity of culture conditions used in the literature (summarized in Figure 2 - Figure supplement 2) makes a direct comparison of the literature data difficult and often key parameters, such as specific growth rate, spectral properties of the light source, vessel geometry or gas exchange rates are not reported in sufficient detail. The premise of this study was therefore to use a highly reproducible cultivation setup that enables stable culture conditions in turbidostat mode and to provide a broad characterization of physiological parameters that can be compared to reported literature values. The results, interpreted in the context of a coarse-grained computational model of cyanobacterial resource allocation, provide further understanding of resource allocation and the cellular protein economy during light-limited, light-saturated and light-inhibited cyanobacterial growth.

Maximal growth rates and glycogen accumulation

The maximal specific growth rates of *Synechocystis* GT-L obtained in this study (Figure 1C, D) were similar to the maximal growth rates of other *Synechocystis* substrains reported in previous studies (***Touloupakis et al., 2015***; ***Nguyen and Rittmann, 2016***; ***Du et al., 2016***; ***Jahn et al., 2018***). While individual *Synechocystis* substrains can be more sensitive to high light (***Zavřel et al., 2017***), the agreement with previously reported values suggests an upper limit of *Synechocystis* growth in buffered BG-11 medium. However, ***van Alphen et al.*** (***2018***) recently reported a specific growth rate of $0.16\mathrm{h}^{-1}$ ($T_D = 4.3\mathrm{h}$) using BG-11 medium with modified iron source and chelating agents. This finding suggests that the standard composition of BG-11 medium still induces a growth limitation, even though in our study the total concentration of iron and other elements refilled during the turbidostat cultivation was sufficient to fully saturate *Synechocystis* growth (Figure 1 - Figure supplement 1).

A sub-maximal specific growth rate in buffered BG-11 medium might also relate to the increase in glycogen content with increasing light intensity and growth rate (Figure 2G, H). The relative amounts of glycogen in *Synechocystis* observed in this study were well within values reported in the literature (Figure 2-Figure supplement 2). However, from the perspective of optimal resource allocation, glycogen accumulation is seemingly suboptimal, since the required energy and carbon is stored and not utilized to enhance growth. Various growth limitations are known to induce accumulation of storage products, including glycogen (***Monshupanee and Incharoensakdi, 2014***), and a recent study showed that glycogen plays an important role in energy balancing and energy homeostasis in *Synechocystis* (***Cano et al., 2018***). We therefore hypothesize that the observed increase in glycogen content, in the absence of other stress factors, is consistent with a limitation in buffered BG-11 medium. This hypothesis is also supported by varying amounts of glycogen reported for the fast-growing strain *Synechococcus elongatus* UTEX 2973: while ***Abernathy et al.*** (***2017***) only report $1.5 \pm 0.5\%$ glycogen of dry weight under fastest growth conditions, ***Ungerer et al.*** (***2018***) report a drastic increase in glycogen content when entering the linear growth phase, and ***Tan et al.*** (***2018***) report up to 54.9% glycogen of dry weight under high light conditions (but unknown growth rate) — suggesting that glycogen accumulation is indicative of growth limitation by other factors than light and carbon availability.

The true growth limit of *Synechocystis* (and other cyanobacteria) remains an open question. Compared to the fast growing strain *Synechococcus elongatus* UTEX 2973, the strain used in this study showed substantially lower carbon partitioning into protein content (23-40% of dry weight, compared to 50% in *Synechococcus* 2973), and increased carbon partitioning into glycogen (8.4-22.9% of dry weight, compared to 1.5% in *Synechococcus* 2973 during the fastest growth (***Abernathy et al., 2017***)). The *Synechocystis* substrain GT-L used here also maintained a lower PSI/PSII ratio (1.35 compared to 2 - 3.5 in *Synechococcus* 7942 and even higher in *Synechococcus* 2973 (***Ungerer et al., 2018***)) and did not increase the amount of electron transport carriers such as plastocyanin

(Kruskal-Wallis test: $p - value = 0.731$) or cytochrome b_6f (Kruskal-Wallis test: $p - value = 0.493$) with increasing light intensity and growth rate. All these factors may contribute to relatively slower growth compared to the fastest growing cyanobacteria. In particular, the recent studies of ***Ungerer et al.*** (***2018***) and ***Abernathy et al.*** (***2017***) demonstrate how just a few mutations in genetically very similar strains can lead to dramatic growth differences — differences that are likely due to different, but as yet not fully understood, cellular strategies in resource allocation. We note, however, that the main goal of our study was not to maximize cyanobacterial growth per se, but to understand resource allocation in a widely used model strain.

We also note that many of the commonly used strains, including substrains of *Synechocystis* sp. PCC 6803, have been maintained in laboratories and in culture collections for extended periods of time, and may have therefore acquired mutations that enhance viability in the lab, but concomitantly reduce maximal growth rates. Indeed, an instance where a cyanobacterial model strain appears to have lost, through laboratory domestication, behaviors that are important in a natural environment was recently reported (***Yang et al., 2018***).

Cell morphology and variability of physiological parameters

Overall, the morphology and range of physiological data obtained in this study were in good agreement with previously published values for *Synechocystis* (see Figure 2 - Figure supplement 1 and Table 2 for detailed comparison). The cell diameter and volume (Figure 2A, B) were well within the range of values reported in the literature (***Lea-Smith et al., 2016***; ***Zavřel et al., 2017***; ***Rosana et al., 2012***). Likewise, the photosynthetic quotient PQ was well within values reported in the literature (***Zavřel et al., 2017***; ***Shastri and Morgan, 2005***) and did not vary significantly with growth rate. The total protein content reported here ($23 - 40\%$ of gDW, Figure 2I) was lower than in several previous studies (***Touloupakis et al., 2015***; ***Shastri and Morgan, 2005***).

As noted above, variability in physiological parameters observed in the literature (Figure 2 - Figure supplement 1, Table 2) can often be attributed to differences in cultivation setup, including selection of particular *Synechocystis* substrain (***Morris et al., 2016***; ***Zavřel et al., 2017***). Additionally, the choice of analytical technique can affect the results, especially with respect to absolute quantification. We are aware of limitations of some techniques used in this work, including glycogen estimation (where the extracellular polymeric substances can potentially lead to overestimation of glycogen content), proteins extraction (where some proteins, especially those with transmembrane domains, could be potentially extracted with reduced efficiency), total protein quantification (where bovine serum albumin, used as a protein standard, does not have to represent cyanobacterial proteins properly), quantification of individual proteins (where the mass spectrometer ionization efficiency could potentially be affected for proteins with lower amount of charged amino acid), relative DNA estimation by flow cytometry (where penetration of SYBR® Green I solution to the cells as well as SYBR® Green I binding to RNA could both potentially differ under increasing light intensity), or phycobiliproteins determination (where proteomics analysis resulted in two times higher values than spectrophotometric analysis, Table 2). Nevertheless, even taken these technical limitations into account, the quantities reported here fit well into the previously reported ranges of *Synechocystis* physiology (Figure 2 - Figure supplement 1, Table 2), as well as to the predictions of the proteome allocation model (Figure 6).

Trends in physiological parameters

Of particular interest were the trends of physiological parameters with respect to increasing light intensity and growth rate. Almost all identified parameters showed significant changes in dependence of light intensity and growth rate, including cell size (diameter and volume , Figure 2A), gas exchange rates (Figure 2C-F), as well as glycogen (Figure 2G-H), DNA and pigment content (Figure 2K-N). Trends in physiological parameters were consistent with previous studies. The increase in gas exchange (O_2 release and basal respiration) has been observed previously (***Zavřel et al., 2015b***, ***2017***). Likewise, the increase in cellular size with growth rate (Figure 2A) has been

reported in *Synechocystis* (***Zavřel et al., 2017***; ***Cordara et al., 2018***) as well as in bacteria, yeast or mammalian cells (***Aldea et al., 2017***). Light was also shown to affect DNA content (ploidy level) in *Synechocystis* (***Zerulla et al., 2016***), however, no study of DNA content change with growth rate is available to date.

Reduction of light harvesting pigments under high light is well documented in the literature. Interestingly, we found upregulation of chlorophyll *a*, phycobilins and both PSII and PSI proteins synthesis in *Synechocystis* cells in the initial part of the growth curve (i.e. between light intensities of 27.5 – 220 µmol(photons) $m^{-2}s^{-1}$, Figure 2L, N, Figure 6C). Similar trends have been described in *Synechocystis* (***Zavřel et al., 2017***) as well as in other cyanobacteria and algae (***Kumar et al., 2011***; ***Wu et al., 2015***). Different from most previous studies, the range of light intensities tested here also included conditions of photoinhibition. In several parameters, in particular glycogen content (Figure 2G-H) or pigment content (Figure 2K-N), we observed a characteristic "kink", i.e., a sharp in- or decrease of the respective abundances. This finding emphasizes photoinhibition as a distinct growth regime and distinguishes phototrophic growth laws from their heterotrophic counterparts.

Our findings also emphasize the need to specify to which reference value the particular changes are reported. Typically, values in the literature are reported relative to optical density as a proxy for cellular dry weight—making a direct comparison between experimental conditions difficult. Furthermore, if cellular composition or cell size changes, these changes do not necessarily translate into corresponding changes per cell or per protein content.

Proteome allocation with growth rate

Beyond physiological parameters, we followed the global proteome allocation as a function of growth rate. The most pronounced changes in proteome with increasing light intensity and growth rate were related to upregulation of translational proteins and downregulation of photosynthetic proteins (Table 1, Figure 6). The upregulation of proteins related to translation (Figure 6B-C) is consistent with well-established growth laws for heterotrophic growth. In particular, *E. coli* shows consistently increased proteome investment into translation-related proteins with increasing growth rate (***Peebo et al., 2015***). Unique for photosynthetic organisms, we observed a decrease of (relative) allocation to proteins annotated with photosynthesis (Figure 6B-C). These results are also consistent with a recent study from ***Jahn et al.*** (***2018***). Likewise, the observed decrease is also in agreement with predictions from resource-allocation models (***Burnap, 2015***; ***Faizi et al., 2018***), even for rather simple models that do not consider photoinhibition (***Burnap, 2015***). While the RbcL subunit of RuBisCo showed a slight increase with increasing growth rate (Figure 6C), we observed no general upregulation of metabolic proteins with increasing growth rate (Figure 6B)—an important deviation from known growth rate relations (***Molenaar et al., 2009***). This finding indicates that the metabolic capacity itself is sufficient for high growth rates, even under conditions where lack of light input limits faster growth. We hypothesize that the most pronounced changes with changing light intensity are observed for proteins related to translation and photosynthesis due to two facts: Firstly, translation is typically limited by ribosomal capacity, requiring an upregulation of translational capacity with faster growth rates. In addition, the short half-life of the D1 protein requires the cell to adjust the translational capacity at high light intensities. Secondly, overcapacity of light harvesting may give rise to detrimental effects, such as increased cellular (photo-)damage. In comparison, overcapacity in the metabolic dark reaction does not entail obvious detrimental consequences (other than the loss of the invested resources) and therefore might be under less evolutionary pressure to change with changing light intensity. We can further corroborate this hypothesis in silico using the proteome allocation model: by artificially forcing a constant mass fraction of a proteome class, we are able to evaluate the impact of such sub-optimal adaptation on the specific growth rate as a function of light intensities. While constant mass fractions of ribosomal and photosynthetic proteins results in a marked deviation in the specific growth rate, a constant metabolic fraction only results in a minor deviation (Figure 6-Figure supplement 2).

Interpretation of the results in the context of a coarse-grained model

The coarse-grained model of phototrophic growth allows us to interpret the physiological and proteomic changes in the context of (optimal) protein allocation. We emphasize that the model was not constructed or parametrized to reproduce certain observed behavior – rather it represents an independent null-hypothesis that provides information about the expected changes in proteome fractions with increasing growth rate under the assumption of (evolutionary) optimality. In line with models of heterotrophic growth (***Molenaar et al., 2009***; ***Weiße et al., 2015***), the model predicts an increase in allocation of ribosomal proteins as a function of growth rate (Figure 6B-C). Different to heterotrophic models, however, the model also predicts a characteristic upward "kink" under conditions of photoinhibition. The relative proteomics data confirms this behavior, including the "kink" at high light intensities (Figure 6B-C). The sharp upregulation of ribosomes in the model is due to the increased turnover of proteins subject to photodamage. As previously noted in (***Faizi et al., 2018***), the model is likely to overestimate this effect, due to the fact that within the model, photodamage is exclusively related to an increase in protein turnover. We expect that in *Synechocystis* also other repair mechanisms are active, resulting in a less pronounced upregulation of ribosomes and energy usage elsewhere. Indeed, the observed upregulation in the data is less pronounced than in the model simulations (Figure 6B-C). Furthermore, the model predicts a downregulation of the light harvesting machinery with increasing light intensity (Figure 5B) and growth rates (Figure 6B-C). The relative proteome allocation confirms this trend, including again the predicted "kink" when entering photoinhibition (Figure 6B-C). Interestingly, the characteristic "kinks" were not observed in the recent study of ***Jahn et al.*** (***2018***) — possibly because the experimental condition used therein only considered a single light condition in the photo-inhibited growth regime.

Finally, as for models of heterotrophic growth, the model predicts an increase in the proteome fraction related to metabolic processes with increasing growth rate (Figure 6B-C). The metabolic proteome fraction, in particular enzymes related to a genome-scale metabolic reconstruction (***Knoop et al., 2013***), did not exhibit such a clear upregulation with the exception of the RbcL protein (a subunit of RuBisCo) that increased in relative abundance with increasing growth rate (Figure 6C). We note that, different from our results, the recent study of ***Jahn et al.*** (***2018***) reported an increase in the metabolic proteome fraction with increasing light intensity, albeit also less than expected compared to the computational growth model.

There are several possible reasons for discrepancies between the model predictions and observed data. In the case of metabolic proteins, a possible factor, besides the hypothesis outlined above, is that the enzymatic reactions are typically not only limited by enzyme abundance, but also by substrate availability. That is, substrate concentration below the respective Michaelis half-saturation constants imply a (seemingly) superfluous enzyme capacity — and hence less requirement to regulate enzyme abundance as a function of growth rate. In addition, discrepancies between model and observed data can be expected when other factors play a role in resource allocation, such as diurnal light availability (***Reimers et al., 2017***) or bet-hedging (i.e. a trade-off between a reduction in growth rate in the present condition in exchange for resource allocation into proteins that are potentially beneficial in future conditions).

Conclusions

Despite the importance of cyanobacteria as photosynthetic model organisms and as host organisms for green biotechnology, as yet only few studies have addressed quantitative growth properties and resource allocation even for well characterized model strains. The goal of this study was therefore to close this gap with respect to knowledge and interpretation of key physiological parameters of the cyanobacterial model strain *Synechocystis* sp. PCC 6803 in dependence of light intensity and growth rate. We focused on light as the only variable environmental parameter – and identified trends in key physiological parameters and proteome allocation as a function of growth rate. The interpretation of data was facilitated by a coarse-grained computational model of cyanobacterial resource allocation and the data was put into the context of data available in

the literature, obtained by a comprehensive literature research. Overall, the resulting growth laws (decrease of proteome fraction associated with light harvesting and increase of proteome fraction associated with translation and biosynthesis with increasing light intensity and growth rate) is in good agreement with previous theoretical (***Burnap, 2015***; ***Faizi et al., 2018***) and experimental studies (***Jahn et al., 2018***).

Light, however, is not the only factor that affects photoautotrophic growth. Further studies are required to identify growth limitation under different environmental conditions, in particular limitations induced by other biotechnologically or environmentally relevant macro- or micronutrients. Ultimately, such studies will also have to take into account the diversity of cyanobacterial metabolism (***Beck et al., 2018***). As indicated by the rather minor genetic differences between strains with vastly different growth rates, we expect that differences in many biotechnologically relevant parameters between strains are indeed a consequence of different strategies in resource allocation — making further studies of cellular accounting a key prerequisite for successful green biotechnology. The proposed reproducible cultivation setup and the coarse-grained computational model used in this study provide a suitable framework and reference to facilitate and to contribute to such studies.

Materials and Methods

Inoculum cultures

Synechocystis sp. PCC 6803 GT-L was obtained from Prof. D. A. Los (Timiryazev Institute of Plant Physiology, Moscow, RU). The strain was cultivated in BG-11 medium (***Stanier et al., 1971***) supplemented with 17 mM HEPES (Carl Roth, Karlsruhe, Germany, pK_a = 7.5). pH of the buffered BG-11 was adjusted to 8.2. The inoculum cultures were precultivated in 250-mL Erlenmeyer flasks on a standard orbital shaker (120 rpm) in a cultivation chamber tempered at 25°C under an average illumination of 110 µmol(photons) $m^{-2}s^{-1}$ (provided by cool white light LEDs) and under 1% CO_2 in the atmosphere.

Photobioreactor

Growth experiments were performed in flat panel photobioreactors, described in detail previously (***Nedbal et al., 2008***). The illumination in the photobioreactors was designed as a chessboard configuration of red and blue LEDs (red: $\lambda_{max} \approx 633$ nm, $\lambda_{1/2} \approx 20$ nm, Luxeon LXHLPD09; blue: $\lambda_{max} \approx 445$ nm, $\lambda_{1/2} \approx 20$ nm, Luxeon LXHL-PR09; all manufactured by Future Lighting Solutions, Montreal, QC, Canada). Spectral characteristics of the LEDs are shown in ***Zavřel et al. (2015b)***. The photobioreactor continuously measured optical density (OD) by an inbuilt densitometer and steady-state pigment fluorescence emission yield by an inbuilt fluorometer (both described in ***Nedbal et al. (2008)***). Dissolved O_2 was monitored by the InPro6800 electrode, culture temperature and pH were monitored by the InPro3253 electrode (all manufactured by Mettler-Toledo Inc., Columbus, OH, USA). Culture homogenization was secured by the inflow gas bubbling with a rate of 200 mL min^{-1}, complemented by rotations of a magnetic stirrer bar (ϕ5 × 35 mm, 210 rpm) in a vertical plane. All other photobioreactor accessories were the same as described in (***Zavřel et al., 2015b***). The photobioreactor setup is visualized in Figure 1A.

Experimental setup

Growth characterization was performed in a quasi-continuous regime as described previously (***Zavřel et al., 2015b***). Briefly, the exponentially growing *Synechocystis* cells were maintained in a defined range of optical density (measured at 680 nm, OD_{680}) by controlled dilution of the culture suspension with fresh buffered BG-11 medium (turbidostat). The optical density was measured by the photobioreactor instrument base, and the OD_{680} range was set to 0.60 - 0.66, which corresponded to approximately 2 – 4 x 10^7 cells mL^{-1}. Starting OD_{680} of all cultures was 0.1 - 0.2, which corresponded to approximately 2 - 4 x 10^6 cells mL^{-1}. Once the culture density reached OD_{680} 0.66, the

quasi-continuous cultivation setup was initiated by starting automated cultures dilution within the selected OD_{680} range. Under each light condition, the cultures were growing for at least 24 hours. This period was long enough to reach growth stability, i.e. to acclimate the cells to the specific condition. The principal of quasi-continuous cultivation is represented in Figure 1B.

During the quasi-continuous experiments, *Synechocystis* was cultivated under red light intensities of 27.5 – 1000 µmol(photons) $m^{-2}s^{-1}$. The cultures were always supplemented with low intensity of blue light (27.5 µmol(photons) $m^{-2}s^{-1}$) in order to avoid growth limitation by complete absence of short wavelength photons (***Golden, 1995***). Cultivation temperature was set to 32°C, and the experiments were performed under a CO_2 concentration of 5000 ppm in the sparging gas (secured by the Gas Mixing System GMS 150, Photon System Instruments Ltd., Brno, CZ).

Analytical methods

Growth rates determination

Specific growth rates μ were evaluated from an increase of OD_{680} signal as recorded by the photobioreactor during the quasi-continuous cultivation (after the growth stabilized under each particular light intensity), according to ***Zavřel et al.*** (***2015b***):

$$\mu = \frac{ln\frac{OD_{680\ t_2}}{OD_{680\ t_1}}}{t_2 - t_1}\ , \tag{1}$$

where $OD_{680\ t_1}$ and $OD_{680\ t_2}$ represent optical densities measured at 680 nm in times t_1 and t_2, respectively. As an alternative method, specific growth rates were determined from depletion of spare cultivation medium, as measured by top loading balances (Ind231, Mettler-Toledo Inc., Columbus, OH, USA, Figure 1C), according to the following equation:

$$\mu = \frac{f}{V}\ , \tag{2}$$

where f represents average flow rate of spare cultivation medium and V represents volume of the culture suspension in the photobioreactor.

Determination of photosynthesis and respiration rates

The oxygen evolution rates as a sum of all oxygen fluxes between *Synechocystis* cells and cultivation media (net photosynthesis, NP) and dark respiration rates (R) were determined from the signal of dO_2 electrode in the photobioreactor vessel by turning off aeration for 10 min, through 5 min light and 5 min dark periods, according to ***Červený et al.*** (***2009***). Gross photosynthesis rates (rates of oxygen production by water splitting, GP) were calculated as: GP = NP + R (photorespiration and other processes were neglected for the GP calculations).

Carbon uptake (net CO_2 uptake rate as a sum of all CO_2 fluxes between *Synechocystis* cells and cultivation media) was determined from the steady-state values of CO_2 concentration in the photobioreactor output gas, as measured by the Gas Analyzing System (Photon System Instruments Ltd., Brno, CZ, described in detail in ***Červený et al.*** (***2009***)).

Pigment content measurements

Content of chlorophyll *a*, carotenoids and phycobilisomes was measured spectrophotometrically following the protocols of ***Zavřel et al.*** (***2015a***) and ***Zavřel et al.*** (***2018a***).

Measurements of glycogen, cell size and DNA content

Content of glycogen was measured spectrophotometrically, following the protocol of ***Zavřel et al.*** (***2018b***). Cellular dry weight was measured using XA105DR analytical balances (Mettler Tolledo, Greifensee, CH). Cell count was measured with the Cellometer Auto M10 (Nexcelom Bioscience, Lawrence, MA, USA).

Cell size was determined using the ImageStream MkII imaging flow cytometer (Amnis Corp., Seattle, WA, USA). Right after harvesting from the photobioreactor, 500 µL of the culture suspension was centrifuged (4 000 g, 4 min, 25°C), supernatant was discarded, pellet was resuspended in 0.25% glutaraldehyde solution and the samples were incubated for 10 min at laboratory temperature. The fixed cells were stored in -80°C until further processing (up to 2 months in total). For further analysis, the samples were thawed on ice for 2 hours, and they were kept at laboratory temperature in dark for additional 30 min after thawing (after 20 min, 5 µL of SYBR® Green I solution was added to each sample for DNA content estimation; for details see the next paragraph). During the cytometric analysis, only bright field images were collected by the imaging flow cytometer. Gating of the measured populations was applied to discriminate: a) focused objects (using combination of both RMS gradient and Treshold Mask features of IDEAS® software), and b) round objects (width/length ratio between 0.9 – 1.0). The imaging flow cytometer was calibrated with non-fluorescent microspheres (1 – 15 µm, Thermo Fisher Scientific, Waltham MA, USA) and the results were validated with the light microscope Axio Imager 2 (Carl Zeiss, Oberkochen, DE). During the cytometric analysis, also chlorophyll fluorescence (excitation: 488 nm, detection: 480 - 560 nm) and phycobilisomes fluorescence (excitation: 642 nm, detection: 642 nm - 745 nm) were measured to validate selection of the cells within all measured objects.

DNA content was measured in the same samples as the cell size. After the samples thawing on ice for 2 hours and at laboratory temperature for 20 min (see the previous paragraph for details), 5 µL of SYBR® Green I solution (Thermo Fisher Scientific, Waltham, MA USA, diluted 1:100 in DMSO) was added to 500 µL of the culture suspension to mark cellular DNA, and the samples were further incubated for 10 min in the dark at laboratory temperature. During the cytometric analysis, a 488 nm argon laser was used to excite both SYBR® Green I and chlorophyll *a*, and another 642 nm laser was used to excite phycobilisomes. To identify *Synechocystis* cells within all measured objects, the same gating as described in the previous paragraph was used.

Protein extraction

Protein extraction was performed according to ***Brown et al.*** (***2008***) with modifications. For each sample, 90 mL of the culture suspension was withdrawn from the photobioreactor, centrifuged (4 000 ×g, 5 min, 32°C), supernatant was partially discarded (leaving 0.5 - 1 ml of liquid in the original 50 mL conical tube) and the pellet was resuspended and transferred to 1.5 mL Eppendorf tube. The tubes were centrifuged (20 000 x g, 4 min, 32°C), supernatants were completely discarded and the tubes were stored at -80°C until further processing (up to 4 months). All following steps of protein isolation were performed at 4°C. The frozen pellets were resuspended in 0.8 mL of a protein extraction buffer (50 mM Tris-HCl (pH 7.6); 2 mM EDTA; 10 mM $MgCl_2$; 250 mM sucrose, 1% of protease inhibitor cocktail P9599, Sigma-Aldrich, St. Louis, MO, USA). The mixture was transferred to 2mL tubes with a rubber o-ring (containing 0.5 mL of sand and glass beads) and the cells were disrupted by 6 x 30 s homogenization pulses on the laboratory mixer (BeadBug Microtube Homogenizer, Benchmark Scientific, Sayreville, NJ, USA). Between each pulse, the samples were kept on ice. After the first step of homogenization, the samples were shortly centrifuged, 200 µL of 10% SDS was added to each tube (to reach the final concentration of 2%), and the samples were mixed and frozen in liquid nitrogen. Right after freezing, the cells were additionally sonicated in an ultrasound bath with ice until thawing (6 cycles, between each cycle the samples were frozen in liquid nitrogen). After ultrasound homogenization, the samples were centrifuged (10 000 x g, 3 min, 4°C) to remove unbroken cells and cell debris, and 500 µL of the supernatant protein fraction was transferred to a new 1.5 mL Eppendorf tube. The total protein concentration was measured in triplicates with a bicinchoninic acid assay kit (BCA1-1KT, Sigma-Aldrich, USA) by the method of ***Smith et al.*** (***1985***) using bovine serum albumin (A7906, Sigma-Aldrich, USA) as a standard. The samples were used for both immunoblotting and proteomics measurements.

Immunoblotting protein analysis

Immunoblotting and protein quantification was done according to ***Brown et al.*** (***2008***) with modifications. 100 µl of each sample was diluted with equal volume of 2x loading buffer (100 mM Tris-HCl (pH 7.6); 20 mM DTT, 4% SDS 0.02% bromphenol blue, 20% glycerol), denatured for 20 min at 37°C and centrifuged (10 000 x g, 20 min, laboratory temperature) before loading. Samples containing 4 µg of total protein were separated in 12.5% (for detection of RbcL, S1, L1) or 15% (for detection of D1, PsaC) 0.75 mm thick polyacrylamide mini gels by SDS-PAGE at 200 V for 40-50 min in a MiniProtean Tetra Cell (Bio-Rad, Hercules, CA, USA). Separated proteins were transferred to 45 µm nitrocellulose membranes (Hybond-C Extra, GE Healthcare Life Sciences, Chicago, Il, USA) using the Trans-Blot Turbo Transfer system (BioRad, Hercules, CA, USA) at 25 V, 1.0 A, laboratory temperature, and cycle duration of 30 min. The nitrocellulose membranes were blocked immediately after transfer in TBST-G buffer (10 mM Tris-HCl (pH7.6); 150 mM NaCl; 0.05% (v/v) Tween-20; 1% cold-water fish gelatin) for 2h at laboratory temperature. Primary antibodies diluted in TBST-G buffer were used according to recommendations of the manufacturer. The list of primary antibodies is provided in Figure 6-Figure supplement 1. After incubation of the membranes in the primary antibody solutions for 1h at laboratory temperature, the solutions were poured off and the membranes were briefly rinsed and washed 3 times for 15 min in TBST buffer at laboratory temperature. For signal detection, the membranes were incubated with goat anti-rabbit immunoglobulin G horseradish peroxidase conjugated antibodies diluted 1:75000 in TBST buffer for 1 h at laboratory temperature. Membranes were washed as described above and developed with Clarity Western ECL Substrate (Bio-Rad, Hercules, CA, USA) according to the manufacturer's instructions. Images of the blots were obtained using a Gel Doc XR+ system (Bio-Rad, Hercules, CA, USA).

Intensity of protein bands on immunoblots was estimated by densitometric analysis with the Image Lab 5.1 software (Bio-Rad, Hercules, CA, USA). The protein concentrations were quantified as relative to the lowest light intensity (27.5 µmol(photons) $m^{-2}s^{-1}$). In addition, absolute amounts of PsbA, PsaC, and RbcL proteins were estimated from standard curves prepared by serial dilutions of corresponding standard proteins. The list of protein standards is provided in Figure 6-Figure supplement 1.

Quantitative proteomics

Protein lysates of 5 individually grown replicate samples per group (27.5-55-110-220-440-1100 µmol(photons) $m^{-2}s^{-1}$) were prepared for mass spectrometric analysis by shortly stacking 5 µg proteins per sample in a 4-12% Bis-Tris sodium dodecyl sulfate (SDS)-polyacrylamide gel (Thermo Scientific, Darmstadt, Germany) over a 4 mm running distance. Proteins were further processed as described previously (***Poschmann et al., 2014***). Briefly, gels were subjected to a silver staining protein containing bands cut out from the gel, destained, washed, reduced with dithiothreitol and alkylated with iodoacetamide. Subsequently, proteins were digested for 16 h at 37°C with 0.1 µg trypsin (Serva, Heidelberg, Germany), peptides were extracted from the gel and after drying in a vacuum concentrator resuspended in 0.1% trifluoroacetic acid. 500 ng of sobulized peptides per sample were then analyzed by a liquid chromatography (Ultimate 3000 Rapid Separation Liquid Chromatography system, RSLC, Thermo Fisher Scientific, Dreieich, Germany) coupled with quantitative mass spectrometry. First, peptides were loaded for 10 minutes at a flow rate of 6 µl/min on a trap column (Acclaim PepMap100 trap column, 3 µm C18 particle size, 100 Å pore size, 75 µm inner diameter, 2 cm length, Thermo Fisher Scientific, Dreieich, Germany) using 0.1 % trifluoroacetic acid as mobile phase. Subsequently, peptides were separated at 60°C on an analytical column (Acclaim PepMapRSLC, 2 µm C18 particle size, 100 Å pore size, 75 µm inner diameter, 25 cm length, Thermo Scientific, Dreieich, Germany) at a flow rate of 300 nl/min using a 2 h gradient from 4 to 40% solvent B (solvent A: 0.1% (v/v) formic acid in water, solvent B: 0.1% (v/v) formic acid, 84% (v/v) acetonitrile in water).

Separated peptides were injected via distal coated SilicaTip emitters (New Objective, Woburn, MA, USA) into a Q Exactive plus Orbitrap mass spectrometer (Thermo Fisher Scientific, Dreieich,

Germany) online coupled via a nanosource electrospray interface. The mass spectrometer was operated in data dependent positive mode with a capillary temperature of 250°C and spray voltage set to 1 400 V. First, full scans were recorded in profile mode at a resolution of 70 000 over a scan range from 350 to 2 000 m/z. Ions were accumulated for a maximum of 80 ms and the target value for automatic gain control was set to 3 000 000. Second, a maximum of ten two- or threefold charged precursor ions were selected within a 2 m/z window using the build in quadrupole, fragmented via higher-energy collisional dissociation and fragments analyzed in the Orbitrap over a maximal scan range from 200 to 2 000 m/z at a resolution of 17 500. Here, the automatic gain control was set to 100 000 and the maximum ion time was 60 ms. For the next 100 s already fragmented precursors were excluded from further analysis.

Peptide and protein identification

For peptide and protein identification and quantification the MaxQuant software suite (version 1.6.1.0, MPI for Biochemistry, Planegg, Germany) was used with standard parameters if not otherwise stated. For database searches 3507 protein entries from the UP000001425 *Synechocystis* sp. strain PCC 6803 downloaded on the 20th of November 2017 from the UniProtKB were considered. Searches were conducted using following parameters: carbamidomethylation at cysteines as fixed and oxidation at methionine and N-terminal protein acetylation as variable modification, false discovery rate on peptide and protein level 1%, match between runs enabled as well as label-free quantification and iBAQ, tryptic cleavage specificity with a maximum of two missed cleavage sites. A first search was conducted with a precursor mass tolerance of 20 ppm and after recalibration by MaxQuant, 4.5 ppm precursor mass tolerances were applied. The mass tolerances for fragment spectra signals were set to 20 ppm.

Quantitative information for identified proteins was further processed within the Perseus framework (version 1.6.1.1, MPI for Biochemistry, Planegg, Germany). Here, only non-contaminant proteins identified with at least two different peptides were considered. Additionally, all proteins were filtered out which - in at least one group – did not show any missing values in the label-free quantification data which then was used after log2 transformation for statistical analysis and relative protein amount comparisons between the different light intensity groups. Calculations of protein stoichiometries and comparison to quantitative protein data derived from other methods was done on absolute quantitative data based on iBAQ intensities. First, iBAQ intensities were normalized on the sum iBAQ intensities of four proteins (Q55806, P72587, P73505, Q59978) showing a small standard deviation, similar intensity range and ratio close to 1 between the mean intensities of the 27.5 and 1100 µmol(photons) $m^{-2}s^{-1}$ group. Second, a calibration of absolute intensities was performed using the PsaC Western blot data (mean of 104 fmol/µl). The mass spectrometry proteomics data have been deposited to the ProteomeXchange Consortium via the PRIDE (***Vizcaíno et al., 2016***) partner repository with the dataset identifier PXD009626.

Proteomaps

For generating proteomaps, the version 1.0 of the visualization tool at www.proteomaps.net (***Liebermeister et al., 2014***) was used, choosing absolute quantitative values and *Synechocystis* sp. 6803 as organism. To be compatible with the proteomaps tool, the mass spectrometric data was searched against the 3661 entries from the GCA_000009725.1 protein dataset from CyanoBase downloaded on 22th January 2018.

Statistical analysis

Kruskal-Wallis test

For the identification of cellular resources that significantly changed with growth rate (including each single protein out of total 1356 identified proteins), we performed a Kruskal-Wallis test (Python scipy.stats module) for each resource (null hypothesis was that the median of all compared groups is equal) and did a pair-by-pair comparison of two conditions in each case. For the test we compared

only those measurements with at least 3 samples. Cellular components and proteins determined as significantly changing with light intensity and growth rate were those that had at least one pair that differed significantly with a $p - value < 0.05$.

Fisher's exact test

We further performed a Fisher's exact test to investigate which of the GO categories filtered out from the proteomics dataset are significantly associated to growth related proteins. For this test we used the GO slim categories. Therefore, we classified the 1356 proteins into growth dependent (779 proteins) and independent groups (577 proteins). The second classification criterion referred to being in one specific gene ontology group or not. The test was then performed for each GO slim category. An imbalance for one GO slim category, between the amount of growth-dependent and growth-independent proteins, was determined as significant for a $p - value < 0.05$.

A coarse-grained proteome allocation model

Model overview

The previously published model of proteome allocation of ***Faizi et al.*** (***2018***) was extended with a growth-independent protein class Q that accounts for approximately half of the proteome. The growth-dependent proteome is comprised of transporter (T), ribosomes (R), metabolic enzymes (M) and photosynthetic units (P). Furthermore, protein degradation and an energy maintenance term were added, resulting in a basal energy expenditure. A description of the modified model with all reaction rates and parameters is provided in Figure 5 and Figure 5-Figure supplement 1.

The proteome allocation model gives rise to an optimization problem. We assume that the objective of a unicellular organism is to maximize its growth rate while the proteome mass remains constant. The maximization of the cellular growth rate, for a given external condition, is achieved by re-adjusting the amount of ribosomes that are delegated to translate a specific protein. The optimization problem was solved using the APMonitor Optimization Suite (***Hedengren et al., 2014***) with the steady-state optimization mode and the IPOPT (Interior Point Optimizer) solver option. The python interface was used to run the model.

Model parametrization and fitting

The model describes growth per cellular dry weight. Cell size only affects the estimated parameter for diffusion of inorganic carbon. For simplicity, the diffusion parameter is set constant (with a cell diameter of approximately 2 µM). Parameters were as in (***Faizi et al., 2018***) and sourced from the primary literature. Only three parameters τ (turnover rate of the photosynthetic unit), k_d (photodamage) and σ (effective absorption cross-section) were then fitted to the measured growth rates. No protein data were used in the fitting. Parameter estimation was done for an external inorganic carbon concentration of c_i^x = 100 mM (c_i^x saturated condition). To minimize the computational effort, a pre-defined set of values for these parameters was specified prior to fitting,

$$\tau = \{50, 75, 100\}\ , \tag{3}$$

$$k_d = \{5 \cdot 10^{-7}, 6 \cdot 10^{-7}, ..., 4 \cdot 10^{-6}, 5 \cdot 10^{-6}\}\ , \tag{4}$$

$$\sigma = \{0.1, 0.2, ..., 0.9, 1\}\ . \tag{5}$$

To select the best fit, the negative logarithm of the likelihood was calculated for each parameter set:

$$l(\theta) = \sum_i \frac{(y_i(\theta) - x_i)^2}{e_i^2} + log(2 \cdot \pi \cdot e_i^2), \tag{6}$$

where x_i represents the here measured growth rates with their uncertainties e_i and $y_i(\theta)$ the simulated growth rates calculated with the model parameters θ. The best fit $l(\theta)$ = -51.46, was obtained with τ = 75 s^{-1}, k_d = 10^{-6} and σ = 0.7 nm^2. Compared to the original model, the addition of the growth-independent protein fraction enhances the energy demand of the cell, and increases the

turnover rate and absorption cross-section of the photosystem. We emphasize that the purpose of the model was not to provide an exact fit to the data, but to guide the interpretation of the results.

Impact of non-adaptive protein fractions on the estimated growth rate

To investigate the potential influence of a constant (non-adaptive) protein mass fraction of Ribosome, Photosynthetic unit, and Metabolic proteins classes (as shown in Figure 6) on the predicted growth rate, an additional constraint was added to the optimization problem, such that the concentration of the respective protein class is

$$[Z] = \frac{\varphi_Z \cdot D_c}{n_Z}\,, \tag{7}$$

where D_c is the cell density (in units of amino acids per cell), n_Z determines the length of the enzyme Z, and φ_Z is the (constant) mass fraction of the protein class Z. In addition, to account for the fact that proteins can be de- or activated (by post-translational modifications such as phophorylation), an additional variable α_Z was introduced that determines the amount of active enzymes (such that the amount of catalytically active enzyme Z_a is $[Z_a] = \alpha_Z \cdot [Z]$). The growth rate is then optimized using the remaining protein classes, as well as the parameter α_Z as variables. The value for the constant protein fraction was set such that it corresponds to the mass fraction of the respective protein class at the highest growth rate.

Acknowledgments

Funding

T.Z and J.Č. were supported by the Ministry of Education, Youth and Sports of the Czech Republic within the National Sustainability Program I (NPU I), grant number LO1415, under OP RDE grant number CZ.02.1.01/0.0/0.0/16_026/0008413 "Strategic Partnership for Environmental Technologies and Energy Production", and by GA CR, Grant number 18-24397S. Access to instruments and facilities was supported by the Czech research infrastructure for systems biology C4SYS (project no. LM2015055). M.F. was supported by the German Research Foundation (DFG), Research Training Group 1772/2 (Computational Systems Biology). A.Z. and M.S. were supported by the Russian Science Foundation, grant number 14-14-00904. G.P. and K.S. were supported by the German Research Foundation (DFG), CRC1208 “Identity and Dynamics of Membrane Systems - from Molecules to Cellular Functions. R.S. was funded by the grant "CyanoGrowth" of the German Federal Ministry of Education and Research as part of the "e:Bio -Innovationswettbewerb Systembiologie" [e:Bio - systems biology innovation competition] initiative (reference: FKZ 0316192).

The funders had no role in study design, data collection and interpretation, or the decision to submit the work for publication.

Author contributions

Tomáš Zavřel, Conceptualization, Project administration, Methodology, Investigation, Formal analysis, Writing—original draft, Writing—review and editing; Marjan Faizi, Investigation, Data curation, Formal analysis, Writing—review and editing; Cristina Loureiro, Investigation, Formal analysis; Gereon Poschmann, Kai Stühler, Methodology, Data curation; Maria Sinetova, Anna Zorina, Methodology, Investigation, Writing—review and editing; Ralf Steuer, Investigation, Conceptualization, Supervision, Writing—original draft, Writing—review and editing; Jan Červený, Conceptualization, Supervision, Project administration, Funding acquisition, Writing—review and editing

References

Abernathy MH, Yu J, Ma F, Liberton M, Ungerer J, Hollinshead WD, Gopalakrishnan S, He L, Maranas CD, Pakrasi HB, Allen DK, Tang YJ. Deciphering cyanobacterial phenotypes for fast photoautotrophic growth via isotopically nonstationary metabolic flux analysis. Biotechnol Biofuels. 2017 Nov; 10:273.

Al-Haj L, Lui YT, Abed RMM, Gomaa MA, Purton S. Cyanobacteria as Chassis for Industrial Biotechnology: Progress and Prospects. Life. 2016 Nov; 6(4).

841 **Aldea M**, Jenkins K, Csikász-Nagy A. Growth Rate as a Direct Regulator of the Start Network to Set Cell Size.
842 Front Cell Dev Biol. 2017 May; 5:57.

843 **van Alphen P**, Najafabadi HA, dos Santos FB, Hellingwerf KJ. Increasing the Photoautotrophic Growth Rate of
844 Synechocystis sp. PCC 6803 by Identifying the Limitations of Its Cultivation. Biotechnol J. 2018; p. 1700764.

845 **Ashburner M**, Ball CA, Blake JA, Botstein D, Butler H, Cherry JM, Davis AP, Dolinski K, Dwight SS, Eppig JT, Harris
846 MA, Hill DP, Issel-Tarver L, Kasarskis A, Lewis S, Matese JC, Richardson JE, Ringwald M, Rubin GM, Sherlock G.
847 Gene ontology: tool for the unification of biology. Nature Genetics. 2000; 25:25–29.

848 **Beck C**, Knoop H, Steuer R. Modules of co-occurrence in the cyanobacterial pan-genome reveal functional
849 associations between groups of ortholog genes. PLoS Genet. 2018 03; 14(3):e1007239.

850 **Berman HM**, Westbrook J, Feng Z, Gilliland G, Bhat TN, Weissig H, Shindyalov IN, Bourne PE. The Protein Data
851 Bank. Nucleic Acids Res. 2000 Jan; 28(1):235–242.

852 **Bernstein HC**, McClure RS, Hill EA, Markillie LM, Chrisler WB, Romine MF, McDermott JE, Posewitz MC, Bryant DA,
853 Konopka AE, Fredrickson JK, Beliaev AS. Unlocking the Constraints of Cyanobacterial Productivity: Acclimations
854 Enabling Ultrafast Growth. MBio. 2016 Jul; 7(4).

855 **Bosdriesz E**, Molenaar D, Teusink B, Bruggeman FJ. How fast-growing bacteria robustly tune their ribosome
856 concentration to approximate growth-rate maximization. FEBS J. 2015; 282(10):2029–2044.

857 **Brown CM**, MacKinnon JD, Cockshutt AM, Villareal TA, Campbell DA. Flux capacities and acclimation costs in
858 Trichodesmium from the Gulf of Mexico. Mar Biol. 2008; 154(3):413–422.

859 **Burnap RL**. Systems and Photosystems: Cellular Limits of Autotrophic Productivity in Cyanobacteria. Frontiers
860 in Bioengineering and Biotechnology. 2015; 3.

861 **Cano M**, Holland SC, Artier J, Burnap RL, Ghirardi M, Morgan JA, Yu J. Glycogen Synthesis and Metabolite Overflow
862 Contribute to Energy Balancing in Cyanobacteria. Cell Rep. 2018 Apr; 23(3):667–672.

863 **Červený J**, Šetlík I, Trtílek M, Nedbal L. Photobioreactor for cultivation and real-time,in-situ measurement of O2
864 and CO2 exchange rates, growth dynamics, and of chlorophyll fluorescence emission of photoautotrophic
865 microorganisms. Eng Life Sci. 2009; 9(3):247–253.

866 **Cordara A**, Re A, Pagliano C, Van Alphen P, Pirone R, Saracco G, Branco dos Santos F, Hellingwerf K, Vasile N.
867 Analysis of the light intensity dependence of the growth of Synechocystis and of the light distribution in a
868 photobioreactor energized by 635 nm light. PeerJ. 2018; 6:e5256.

869 **Du W**, Jongbloets JA, Hernández HP, Bruggeman FJ, Hellingwerf KJ, dos Santos FB. Photonfluxostat: A method
870 for light-limited batch cultivation of cyanobacteria at different, yet constant, growth rates. Algal Research.
871 2016; 20:118–125.

872 **Erickson DW**, Schink SJ, Patsalo V, Williamson JR, Gerland U, Hwa T. A global resource allocation strategy governs
873 growth transition kinetics of Escherichia coli. Nature. 2017 Nov; 551(7678):119–123.

874 **Faizi M**, Zavřel T, Loureiro C, Červený J, Steuer R. A model of optimal protein allocation during phototrophic
875 growth. Biosystems. 2018 Apr; 166:26–36.

876 **Fujisawa T**, Narikawa R, Maeda SI, Watanabe S, Kanesaki Y, Kobayashi K, Nomata J, Hanaoka M, Watanabe M,
877 Ehira S, Suzuki E, Awai K, Nakamura Y. CyanoBase: A large-scale update on its 20th anniversary. Nucleic Acids
878 Research. 2017; 45(D1):D551–D554. doi: 10.1093/nar/gkw1131.

879 **Golden SS**. Light-responsive gene expression in cyanobacteria. J Bacteriol. 1995; 177(7):1651–1654.

880 **Hedengren JD**, Shishavan RA, Powell KM, Edgar TF. Nonlinear modeling, estimation and predictive control in
881 APMonitor. Computers & Chemical Engineering. 2014; 70:133 – 148. Manfred Morari Special Issue.

882 **Ikeuchi M**, Tabata S. Synechocystis sp. PCC 6803 — a useful tool in the study of the genetics of cyanobacteria.
883 Photosynth Res. 2001; 70(1):73–83.

884 **Jahn M**, Vialas V, Karlsen J, Maddalo G, Forsström FEB, Uhlén M, Käll L, Hudson EP. Growth of Cyanobacteria Is
885 Constrained by the Abundance of Light and Carbon Assimilation Proteins. Cell Reports. 2018; 25:478 – 486.
886 doi: https://doi.org/10.1016/j.celrep.2018.09.040.

887 **Jun S**, Si F, Pugatch R, Scott M. Fundamental principles in bacterial physiology-history, recent progress, and the
888 future with focus on cell size control: a review. Rep Prog Phys. 2018 05; 81(5):056601.

889 **Kafri M**, Metzl-Raz E, Jona G, Barkai N. The Cost of Protein Production. Cell Rep. 2016 Jan; 14(1):22–31.

890 **Keren N**, Aurora R, Pakrasi HB. Critical roles of bacterioferritins in iron storage and proliferation of cyanobacteria.
891 Plant Physiol. 2004 Jul; 135(3):1666–1673.

892 **Klopfenstein DV**, Zhang L, Pedersen BS, Ramírez F, Warwick Vesztrocy A, Naldi A, Mungall CJ, Yunes JM, Botvinnik
893 O, Weigel M, Dampier W, Dessimoz C, Flick P, Tang H. GOATOOLS: A Python library for Gene Ontology analyses.
894 Scientific Reports. 2018; 8(1):10872.

895 **Klumpp S**, Scott M, Pedersen S, Hwa T. Molecular crowding limits translation and cell growth. Proc Natl Acad Sci
896 U S A. 2013 Oct; 110(42):16754–16759.

897 **Klumpp S**, Zhang Z, Hwa T. Growth rate-dependent global effects on gene expression in bacteria. Cell. 2009
898 Dec; 139(7):1366–1375.

899 **Knoop H**, Gründel M, Zilliges Y, Lehmann R, Hoffmann S, Lockau W, Steuer R. Flux Balance Analysis of
900 Cyanobacterial Metabolism: The Metabolic Network of Synechocystis sp. PCC 6803. PLoS Comput Biol.
901 2013; 9(6):e1003081.

902 **Kumar M**, Kulshreshtha J, Singh GP. Growth and biopigment accumulation of cyanobacterium Spirulina platensis
903 at different light intensities and temperature. Brazilian Journal of Microbiology. 2011; 42(3):1128–1135. doi:
904 10.1590/S1517-838220110003000034.

905 **Lea-Smith DJ**, Ortiz-Suarez ML, Lenn T, Nürnberg DJ, Baers LL, Davey MP, Parolini L, Huber RG, Cotton CAR,
906 Mastroianni G, Bombelli P, Ungerer P, Stevens TJ, Smith AG, Bond PJ, Mullineaux CW, Howe CJ. Hydrocar-
907 bons Are Essential for Optimal Cell Size, Division, and Growth of Cyanobacteria. Plant Physiol. 2016 Nov;
908 172(3):1928–1940.

909 **Liebermeister W**, Noor E, Flamholz A, Davidi D, Bernhardt J, Milo R. Visual account of protein investment in
910 cellular functions. Proc Natl Acad Sci U S A. 2014 Jun; 111(23):8488–8493.

911 **Maitra A**, Dill KA. Bacterial growth laws reflect the evolutionary importance of energy efficiency. Proc Natl Acad
912 Sci U S A. 2015 Jan; 112(2):406–411.

913 **Matsumoto Y**, Murakami Y, Tsuru S, Ying BW, Yomo T. Growth rate-coordinated transcriptome reorganization
914 in bacteria. BMC Genomics. 2013 Nov; 14:808.

915 **Metzl-Raz E**, Kafri M, Yaakov G, Soifer I, Gurvich Y, Barkai N. Principles of cellular resource allocation revealed
916 by condition-dependent proteome profiling. Elife. 2017 Aug; 6.

917 **Moal G**, Lagoutte B. Photo-induced electron transfer from photosystem I to NADP(+): characterization and
918 tentative simulation of the in vivo environment. Biochim Biophys Acta. 2012 Sep; 1817(9):1635–1645.

919 **Molenaar D**, van Berlo R, de Ridder D, Teusink B. Shifts in growth strategies reflect tradeoffs in cellular
920 economics. Mol Syst Biol. 2009 Nov; 5:323.

921 **Monshupanee T**, Incharoensakdi A. Enhanced accumulation of glycogen, lipids and polyhydroxybutyrate
922 under optimal nutrients and light intensities in the cyanobacterium Synechocystis sp. PCC 6803. Journal of
923 Applied Microbiology. 2014; 116(4):830–838. https://onlinelibrary.wiley.com/doi/abs/10.1111/jam.12409, doi:
924 10.1111/jam.12409.

925 **Morris JN**, Eaton-Rye JJ, Summerfield TC. Phenotypic variation in wild-type substrains of the model cyanobac-
926 terium Synechocystis sp. PCC 6803. N Z J Bot. 2016; 55(1):25–35.

927 **Mueller TJ**, Ungerer JL, Pakrasi HB, Maranas CD. Identifying the Metabolic Differences of a Fast-Growth
928 Phenotype in Synechococcus UTEX 2973. Sci Rep. 2017 Jan; 7:41569.

929 **Nedbal L**, Trtílek M, Cervený J, Komárek O, Pakrasi HB. A photobioreactor system for precision cultivation of
930 photoautotrophic microorganisms and for high-content analysis of suspension dynamics. Biotechnol Bioeng.
931 2008 Aug; 100(5):902–910.

932 **Neidhardt FC**. Bacterial growth: constant obsession with dN/dt. J Bacteriol. 1999 Dec; 181(24):7405–7408.

933 **Neidhardt FC**, Ingraham JL, Schaechter M. Physiology of the bacterial cell. A Molecular Approach. Sunderland,
934 MA, USA: Sinauer Associates, Inc; 1990.

935 **Nguyen BT**, Rittmann BE. Effects of inorganic carbon and pH on growth kinetics of Synechocystis sp. PCC 6803.
936 Algal Research. 2016; 19:363–369.

Peebo K, Valgepea K, Maser A, Nahku R, Adamberg K, Vilu R. Proteome reallocation in Escherichia coli with increasing specific growth rate. Mol Biosyst. 2015 Apr; 11(4):1184–1193.

Platt T , Gallegos C L , Harrison W G . Photoinhibition of photosynthesis in natural assemblages of marine phytoplankton. J Mar Res. 1980; 38(4):687–701.

Poschmann G, Seyfarth K, Besong Agbo D, Klafki HW, Rozman J, Wurst W, Wiltfang J, Meyer HE, Klingenspor M, Stühler K. High-fat diet induced isoform changes of the Parkinson's disease protein DJ-1. J Proteome Res. 2014 May; 13(5):2339–2351.

Reimers AM, Knoop H, Bockmayr A, Steuer R. Cellular trade-offs and optimal resource allocation during cyanobacterial diurnal growth. Proceedings of the National Academy of Sciences. 2017; 114(31):E6457–E6465.

Rosana ARR, Ventakesh M, Chamot D, Patterson-Fortin LM, Tarassova O, Espie GS, Owttrim GW. Inactivation of a Low Temperature-Induced RNA Helicase in Synechocystis sp. PCC 6803: Physiological and Morphological Consequences. Plant and Cell Physiology. 2012; 53(4):646 – 658. doi: 10.1093/pcp/pcs020.

Rügen M, Bockmayr A, Steuer R. Elucidating temporal resource allocation and diurnal dynamics in phototrophic metabolism using conditional FBA. Sci Rep. 2015 Oct; 5:15247.

Scott M, Gunderson CW, Mateescu EM, Zhang Z, Hwa T. Interdependence of cell growth and gene expression: origins and consequences. Science. 2010 Nov; 330(6007):1099–1102.

Scott M, Hwa T. Bacterial growth laws and their applications. Curr Opin Biotechnol. 2011 Aug; 22(4):559–565.

Scott M, Klumpp S, Mateescu EM, Hwa T. Emergence of robust growth laws from optimal regulation of ribosome synthesis. Mol Syst Biol. 2014 Aug; 10:747.

Shastri AA, Morgan JA. Flux Balance Analysis of Photoautotrophic Metabolism. Biotechnology Progress. 2005; 21(6):1617–1626. doi: 10.1021/bp050246d.

Smith PK, Krohn RI, Hermanson GT, Mallia AK, Gartner FH, Provenzano MD, Fujimoto EK, Goeke NM, Olson BJ, Klenk DC. Measurement of protein using bicinchoninic acid. Anal Biochem. 1985 Oct; 150(1):76–85.

Stanier RY, Kunisawa R, Mandel M, Cohen-Bazire G. Purification and properties of unicellular blue-green algae (order Chroococcales). Bacteriol Rev. 1971 Jun; 35(2):171–205.

Tan X, Hou S, Song K, Georg J, Klähn S, Lu X, Hess WR. The primary transcriptome of the fast-growing cyanobacterium Synechococcus elongatus UTEX 2973. Biotechnology for Biofuels. 2018 Aug; 11(1):218. https://doi.org/10.1186/s13068-018-1215-8, doi: 10.1186/s13068-018-1215-8.

Touloupakis E, Cicchi B, Torzillo G. A bioenergetic assessment of photosynthetic growth of Synechocystis sp. PCC 6803 in continuous cultures. Biotechnol Biofuels. 2015 Sep; 8:133.

Ungerer J, Lin PC, Chen HY, Pakrasi HB. Adjustments to Photosystem Stoichiometry and Electron Transfer Proteins Are Key to the Remarkably Fast Growth of the Cyanobacterium Synechococcus elongatus UTEX 2973. MBio. 2018; 9(1):e02327–17.

UniProt Consortium T. UniProt: the universal protein knowledgebase. Nucleic Acids Res. 2018 Mar; 46(5):2699.

Vázquez-Laslop N, Mankin AS. Protein accounting in the cellular economy. Cell. 2014; 157(3):529–531. doi: 10.1016/j.cell.2014.04.002.

Vizcaíno JA, Csordas A, Del-Toro N, Dianes JA, Griss J, Lavidas I, Mayer G, Perez-Riverol Y, Reisinger F, Ternent T, Xu QW, Wang R, Hermjakob H. 2016 update of the PRIDE database and its related tools. Nucleic Acids Res. 2016 Dec; 44(22):11033.

Weiße AY, Oyarzún DA, Danos V, Swain PS. Mechanistic links between cellular trade-offs, gene expression, and growth. Proc Natl Acad Sci U S A. 2015 Mar; 112(9):E1038–47.

Wu H, Jiang H, Liu C, Deng Y. Growth, pigment composition, chlorophyll fluorescence and antioxidant defenses in the red alga Gracilaria lemaneiformis (Gracilariales, Rhodophyta) under light stress. South African Journal of Botany. 2015; 100:27 – 32. http://www.sciencedirect.com/science/article/pii/S0254629915003038, doi: https://doi.org/10.1016/j.sajb.2015.05.017.

Yang Y, Lam V, Adomako M, Simkovsky R, Jakob A, Rockwell NC, Cohen SE, Taton A, Wang J, Lagarias JC, Wilde A, Nobles DR, Brand JJ, Golden SS. Phototaxis in a wild isolate of the cyanobacterium Synechococcus elongatus. Proc Natl Acad Sci USA. 2018 Dec; .

985 **Yu J**, Liberton M, Cliften PF, Head RD, Jacobs JM, Smith RD, Koppenaal DW, Brand JJ, Pakrasi HB. Synechococcus
986 elongatus UTEX 2973, a fast growing cyanobacterial chassis for biosynthesis using light and CO2. Sci Rep.
987 2015; 5(1).

988 **Zavřel T**, Červený J, Knoop H, Steuer R. Optimizing cyanobacterial product synthesis: Meeting the challenges.
989 Bioengineered. 2016 Nov; 7(6):490–496.

990 **Zavřel T**, Chmelík D, Sinetova MA, Červený J. Spectrophotometric Determination of Phycobiliprotein Content in
991 Cyanobacterium Synechocystis. Journal of Visualized Experiments. 2018a; (139):1 – 9.

992 **Zavřel T**, Očenášová P, Červený J. Phenotypic characterization of Synechocystis sp. PCC 6803 substrains reveals
993 differences in sensitivity to abiotic stress. PLoS One. 2017 Dec; 12(12):e0189130.

994 **Zavřel T**, Očenášová P, Sinetova MA, Červený J. Determination of Storage (Starch/Glycogen) and Total Saccharides
995 Content in Algae and Cyanobacteria by a Phenol-Sulfuric Acid Method. Bio-protocol. 2018b; 8(15):e2966.

996 **Zavřel T**, Sinetova M, Červený J. Measurement of Chlorophyll a and Carotenoids Concentration in Cyanobacteria.
997 BIO-PROTOCOL. 2015a; 5(9).

998 **Zavřel T**, Sinetova MA, Búzová D, Literáková P, Červený J. Characterization of a model cyanobacterium Syne-
999 chocystis sp. PCC 6803 autotrophic growth in a flat-panel photobioreactor. Eng Life Sci. 2015b; 15(1):122–132.

1000 **Zerulla K**, Ludt K, Soppa J. The ploidy level of synechocystis sp. PCC 6803 is highly variable and is influenced
1001 by growth phase and by chemical and physical external parameters. Microbiology (United Kingdom). 2016;
1002 162(5):730–739.

Ratio of the requirements of selected elements by *Synechocystis* cells and the elements supplemented by the replacement of a spare culture medium during turbidostat experiments in this study.								
Red light intensity [µE m^{-2} s^{-1}]	27.5	55	110	220	440	660	880	1100
Na	0.2%	0.4%	0.4%	0.5%	0.4%	0.4%	0.5%	0.5%
N	6.1%	9.6%	10.8%	12.9%	9.7%	11.6%	14.4%	12.7%
Mg	16.8%	26.4%	29.7%	35.6%	26.7%	31.9%	39.7%	35.1%
S	9.4%	14.7%	16.6%	19.9%	14.9%	17.8%	22.2%	19.6%
Ca	20.4%	31.9%	36.0%	43.1%	32.4%	38.6%	48.1%	42.5%
Fe	40.3%	63.1%	71.2%	85.1%	64.0%	76.4%	95.1%	83.9%
P	33.3%	52.2%	58.9%	70.5%	52.9%	63.2%	78.7%	69.5%

Estimated uptake rates of selected elements by *Synechocystis* cells during the turbidostat cultivation [mg L^{-1} h^{-1}]. The calcualtions are based on direct measurements of cellular dry weights and specific growth rates in this study, and on maximal concentration of particular elements in *Synechocystis* biomass as recorded in the literature.								
Red light intensity [µE m^{-2} s^{-1}]	27.5	55	110	220	440	660	880	1100
Na	0.03	0.05	0.08	0.14	0.18	0.21	0.20	0.17
N	0.42	0.80	1.27	2.23	2.89	3.37	3.18	2.69
Mg	0.03	0.07	0.10	0.18	0.24	0.28	0.26	0.22
S	0.03	0.05	0.08	0.14	0.18	0.21	0.20	0.17
Ca	0.06	0.11	0.17	0.30	0.38	0.45	0.42	0.36
Fe	0.01	0.03	0.04	0.07	0.09	0.11	0.10	0.09
P	0.05	0.10	0.15	0.27	0.35	0.40	0.38	0.32

Refilling rates of selected elements during *Synechocystis* cultivation in the turbidostat regime, based on data from this study [mg L^{-1} h^{-1}].								
Red light intensity [µE m^{-2} s^{-1}]	27.5	55	110	220	440	660	880	1100
Na	11.52	14.08	19.71	28.91	49.90	48.78	36.99	35.45
N	6.88	8.41	11.77	17.26	29.80	29.13	22.09	21.17
Mg	0.21	0.25	0.35	0.52	0.89	0.87	0.66	0.63
S	0.28	0.34	0.48	0.70	1.21	1.18	0.89	0.86
Ca	0.27	0.33	0.47	0.69	1.18	1.16	0.88	0.84
Fe	0.03	0.04	0.06	0.08	0.14	0.14	0.11	0.10
P	0.15	0.18	0.26	0.38	0.65	0.64	0.49	0.47

Weights of selected elements in *Synechocystis* cells, based on directly measured cellular dry weight in this study, and on maximal concentration of particular elements in *Synechocystis* biomass as recorded in the literature [mg L^{-1} h^{-1}].								
Red light intensity [µE m^{-2} s^{-1}]	27.5	55	110	220	440	660	880	1100
Na	1.04	1.31	1.37	1.73	1.75	2.05	2.03	1.82
N	16.5	20.7	21.6	27.4	27.7	32.5	32.0	28.9
Mg	1.36	1.71	1.78	2.26	2.28	2.68	2.64	2.38
S	1.03	1.29	1.35	1.71	1.73	2.03	2.00	1.80
Ca	2.19	2.75	2.87	3.64	3.67	4.31	4.26	3.83
Fe	0.53	0.66	0.69	0.88	0.89	1.04	1.03	0.92
P	1.98	2.48	2.59	3.29	3.32	3.90	3.85	3.46

Parameters of *Synechocystis* cultures as measured during the turbidostat experiments in this study.								
Red light intensity used in this study [µE m^{-2} s^{-1}]	27.5	55	110	220	440	660	880	1100
Specific growth rate µ measured in this study [h^{-1}]	0.025	0.039	0.059	0.081	0.104	0.104	0.099	0.093
Flow rate of spare cultivation media measured in this study [h^{-1}]	0.028	0.034	0.048	0.070	0.121	0.118	0.089	0.086
Dry weight of *Synecocystis* cells measured in this study [mg L^{-1}]	132	166	173	220	221	260	256	231

Elemental composition of *Synechocystis* cells based on data available in the literature.					
Element	BG11 [mg L^{-1}]	Content in cell [% of DW] Min	Max	Maximal value recorded in the literature	Reference
Na	413.4	0.1	0.8	0.8	Touloupakis et al. 2016
N	246.9	8.0	11.2	12.5	Zavřel et al. 2017
		10.0	11.1		Touloupakis et al. 2015
		10.2	11.5		Touloupakis et al. 2016
		11.3	11.3		Shastri and Morgan 2005
		12.5			Kim et al. 2011
		7.1	7.7		Blom 2014
S	10.0	0.4	0.8	0.8	Zavřel et al. 2017
		0.4	0.4		Touloupakis et al. 2015
		0.4	0.4		Touloupakis et al. 2016
		0.7			Kim et al. 2011
Ca	9.8	0.3	1.7	1.7	Touloupakis et al. 2016
Mg	7.4	0.4	1.0	1.0	Touloupakis et al. 2016
P	5.4	1.5		1.5	Kim et al. 2011
Fe	1.2	0.1	0.4	0.4	Cheng and He 2014
		0.4			Kim et al. 2011

1003

References:

Blom, M., 2014. The Elemental Composition of *Synechocystis* sp . PCC 6803 under Nutrient Limiting Conditions. Bachelor thesis. University of Amsterdam.

Cheng, D., He, Q., 2014. PfsR Is a Key Regulator of Iron Homeostasis in *Synechocystis* PCC 6803. PLoS One 9, 1–13.

Kim, H.W., Vannela, R., Zhou, C., Rittmann, B.E., 2011. Nutrient acquisition and limitation for the photoautotrophic growth of *Synechocystis* sp. PCC6803 as a renewable biomass source. Biotechnol. Bioeng. 108, 277–285.

Shastri, A. a, Morgan, J. a, 2005. Flux balance analysis of photoautotrophic metabolism. Biotechnol. Prog. 21, 1617–26.

Touloupakis, E., Cicchi, B., Benavides, A.M.S., Torzillo, G., 2016. Effect of high pH on growth of *Synechocystis* sp. PCC 6803 cultures and their contamination by golden algae *(Poterioochromonas* sp.). Appl. Microbiol. Biote

Touloupakis, E., Cicchi, B., Torzillo, G., 2015. A bioenergetic assessment of photosynthetic growth of *Synechocystis* sp. PCC 6803 in continuous cultures. Biotechnol. Biofuels 8, 133.

Zavřel, T., Očenášová, P., Červený, J., 2017. Phenotypic characterization of *Synechocystis* sp. PCC 6803 substrains reveals differences in sensitivity to abiotic stress. PLoS One 12, e0189130.

Figure 1–Figure supplement 1. Uptake and refilling rates of selected nutrients during the quasi-continuous cultivation.

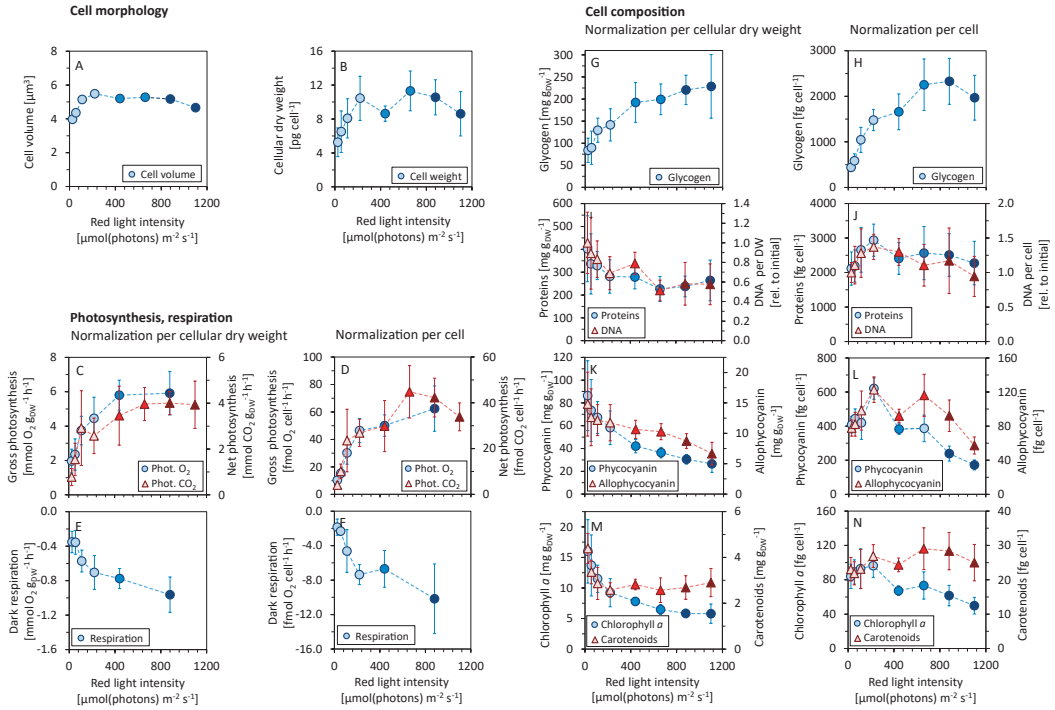

Figure 2–Figure supplement 1. Allocation of key cellular resources as a function of light intensity

Figure 2–Figure supplement 2. Comparison of the values measured in this study with data reported in the literature.

Figure 3–Figure supplement 1. List of growth-dependent proteins.

Figure 3–Figure supplement 2. List of growth-independent proteins.

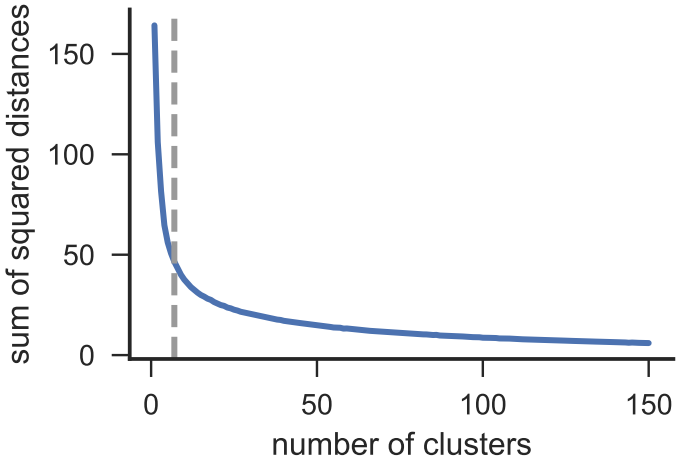

Figure 3–Figure supplement 3. Elbow method for the identification of an appropriate number of clusters (grey dashed line at 7 clusters).

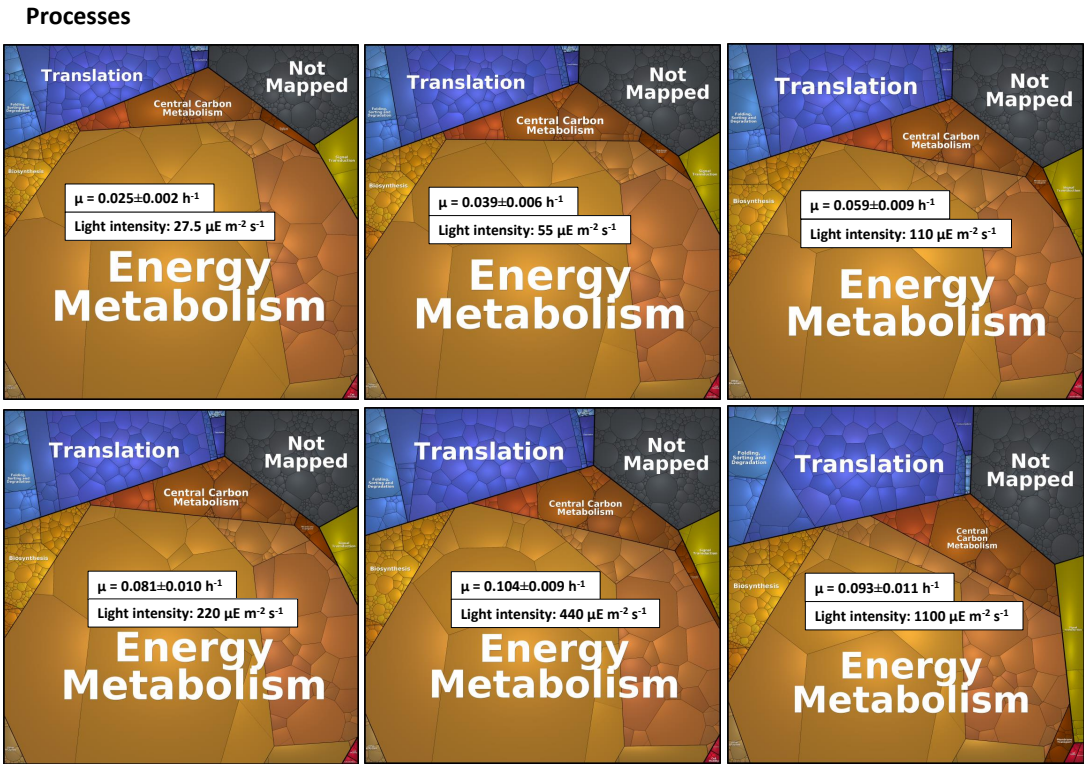

Figure 4–Figure supplement 1. Proteomaps of levels 2, 3 and 4.

SMALL–SCALE PROTEOME ALLOCATION MODEL FOR PHOTOTROPHIC GROWTH

parameter	definition	value	source
P_m	cell membrane permeability to inorganic carbon	0.108 [dm h^{-1}]	(2)
A_{cell}	cell surface area	$1.26 \cdot 10^{-9}$ [dm^2 $cell^{-1}$]	This study
V_{cell}	cell volume	$4.19 \cdot 10^{-15}$ [dm^3 $cell^{-1}$]	This study
N_A	Avogadro constant	$6.022 \cdot 10^{23}$ [mol^{-1}]	
k^t_{cat}	maximal import rate	43560 [h^{-1}]	(3)
K_t	half-saturation constant of the transporter enzyme	15 [µM]	(4)
k^m_{cat}	maximal metabolic rate	32700 [h^{-1}]	(5)
K_m	half-saturation constant of the metabolic enzyme	2441560 [molecules $cell^{-1}$]	(5)
γ_{max}	maximal translation rate	79200 [aa h^{-1} $molecules^{-1}$]	(6)
K_a, K_e	half-saturation constant of amino acids and energy units for each reaction	10000 [molecules $cell^{-1}$]	(1)
d_p	protein half-life	1/23 [h^{-1}]	(7)
σ	effective absorption cross-section of the photosynthetic unit	0.7 [nm^2]	This study
τ	maximal turnover rate of the photosynthetic unit	270000 [h^{-1}]	This study
k_d	rate constant for photodamdage	10^{-6}	This study
m_v	energy maintenance rate	$7 \cdot 10^9$ [molecules $cell^{-1}$ h^{-1}]	(8)
D_c	average cell density (protein mass per cell)	$1.4 \cdot 10^{10}$ [aa $cell^{-1}$]	(1)
n_R	ribosome length	7358 [aa $molecule^{-1}$]	(1)
n_Q	average protein length for house-keeping proteins	300 [aa $molecule^{-1}$]	This study
n_P	length of one photosynthetic unit	95451 [aa $molecule^{-1}$]	(1)
n_T	transporter length	1681 [aa $molecule^{-1}$]	(1)
n_M	length of one metabolic enzyme complex	28630 [aa $molecule^{-1}$]	(1)
m_a	amount of energy units consumed to create one amino acid	45	(1)
m_c	average carbon chain length of an amino acid	5	(1)
m_γ	amount of energy units needed for one translational elongation step	3	(1)
m_ϕ	amount of energy units produced during photosynthesis	8	(1)

Proteome Allocation Problem

$$\max_{\beta,\, X,\, \mu} \quad \mu$$

$$s.t. \; \frac{d[X]}{dt} - \mu \cdot X = 0 \,,$$

$$\sum_j \beta_j = 1 \,, \quad \forall j \in \mathbb{E} : \; \beta_j \geq 0 \,,$$

$$\sum_j n_j \cdot [j] + [aa] + \frac{[c_i]}{m_c} = D_c \,,$$

$$n_Q \cdot [Q] = 0.5 \cdot D_c \,,$$

$$\mathbb{E} = \{R, Q, P, T, M\} \,,$$

$$X = [ci, aa, e, Q, P^O, P^*, T, M, R]^T \in \mathbb{R}_+ \,.$$

ODE System

$$\frac{d[c_i]}{dt} = v_d + v_t - m_c \cdot v_m \,,$$

$$\frac{d[aa]}{dt} = v_m + n_P \cdot v_i - \sum_j n_j \cdot \gamma_j + d_p \cdot \sum_j n_j \cdot [j] \,,$$

$$\frac{d[z]}{dt} = \gamma_z - d_P \cdot [z] \,,$$

$$\frac{d[P^O]}{dt} = \gamma_P - v_1 + v_2 - d_p \cdot [P^O] \,,$$

$$\frac{d[P^*]}{dt} = v_1 - v_2 - v_i - d_p \cdot [P^*] \,,$$

$$\frac{d[e]}{dt} = m_\phi \cdot v_2 - v_t - m_\mu \cdot v_m - m_\gamma \cdot \sum_j n_j \cdot \gamma_j - \frac{m_v \cdot [e]}{10 + [e]} \,,$$

$$\forall j \in \mathbb{E} \,, \forall z \in \mathbb{E} \backslash P \,.$$

Reaction Rates

$$v_d = P_m \cdot \frac{A_{cell}}{V_{cell}} \cdot (N_A \cdot V_{cell} \cdot [c_i^x] - [c_i]) \,,$$

$$v_t = [T] \cdot k^t_{cat} \cdot \frac{[c_i^x]}{K_t + [c_i^x]} \cdot \frac{[e]}{K_e + [e]} \,,$$

$$v_m = [M] \cdot k^m_{cat} \cdot \frac{[c_i]}{K_m + [c_i]} \cdot \frac{[e]}{K_e + [e]} \,,$$

$$\gamma_j = [R] \cdot \beta_j \cdot \frac{\gamma max}{n_j} \cdot \frac{[aa]}{K_a + [aa]} \cdot \frac{[e]}{K_e + [e]} \,,$$

$$v_1 = \sigma \cdot light \cdot [P^O] \,,$$

$$v_2 = \tau \cdot [P^*] \,,$$

$$v_i = k_d \cdot \sigma \cdot light \cdot [P^*] \,,$$

$$\forall j \in \mathbb{E} \,.$$

REFERENCES

1. Faizi M, Zavrel T, Loureiro C, Cerveny J, Steuer R (2018). A model of optimal protein allocation during phototrophic growth. Biosystems 166: 26-36.
2. Mangan NM, Brenner MP (2014). Systems analysis of the CO2 concentrating mechanism in cyanobacteria. eLife 3: p. e02043.
3. Dornmair K, Overath P, Jähnig F (1989). Fast measurement of galactoside transport by lactose permease. J Biol Chem 26(1): 342-346.
4. Omata T, Takahashi Y, Yamaguchi O, Nishimura T (2002). Structure, function and regulation of the cyanobacterial high-affinity bicarbonate transporter, BCT1. Funct Plant Biol 29(3): 151-159.
5. Marcus Y, Altman-Gueta H, Finkler A, Gurevitz M (2005). Mutagenesis at two distinct phosphate-binding sites unravels their differential roles in regulation of Rubisco activation and catalysis. J Bacteriol 187 (12): 222-4228.
6. Bremer H, Dennis P (2008). Modulation of chemical composition and other parameters of the cell at Dif- ferent Exponential Growth Rates. EcoSal Plus, 3(1).
7. Maier T, Schmidt A, Güell M, Kühner S, Gavin AC, Aebersold R, Serrano L (2011). Quantification of mRNA and protein and integration with protein turnover in a bacterium. Mol Syst Biol 7: 511.
8. Knoop H, Gründel M, Zilliges Y, Lehmann R, Hoffmann S, Lockau W, Steuer R (2013). Flux balance analysis of cyanobacterial metabolism: the metabolic network of Synechocystis sp. PCC 6803. PLoS Comput Biol 9(6): e1003081.

Figure 5–Figure supplement 1. Summary of the proteome allocation model.

Table 1. List of antibodies used in this study.

Antibody	Agrisera catalogue number	Dilution	Protein apparent MW
Rabbit Anti-RbcL (Rubisco large subunit, form I and form II)	AS03 037	1:5000	52.5 kDa
Rabbit Anti-PsaC (PSI-C core subunit of photosystem I)	AS10 939	1:1000	9 kDa
Rabbit Anti-PsbA (D1 protein of PSII, C-terminal)	AS05 084	1:10000	28-30 kDa
Rabbit Anti-S1 (30S ribosomal protein S1)	AS08 309	1:2000	35 kDa
Rabbit Anti-L1 (50S ribosomal protein L1)	AS11 1738	1:1000	25 kDa

Table 2. List of protein standards used in this study.

Standard	Agrisera catalogue number	Protein apparent MW	Concentrations
Purified spinach RbcL	AS01 017S	52.7 kDa	0.375, 0.75, 1.5 pmol
Recombinant PsaC from *Synechocystis* PCC 6803	AS04 042S	11.5 kDa	0.075, 0.3, 0.6 pmol
Recombinant PsbA from *Synechocystis* PCC 6803	AS01 016S	41.5 kDa	0.125, 0.5, 1 pmol

Figure 6–Figure supplement 1. Immunoblots and a list of antibodies used for the immunoblotting analysis.

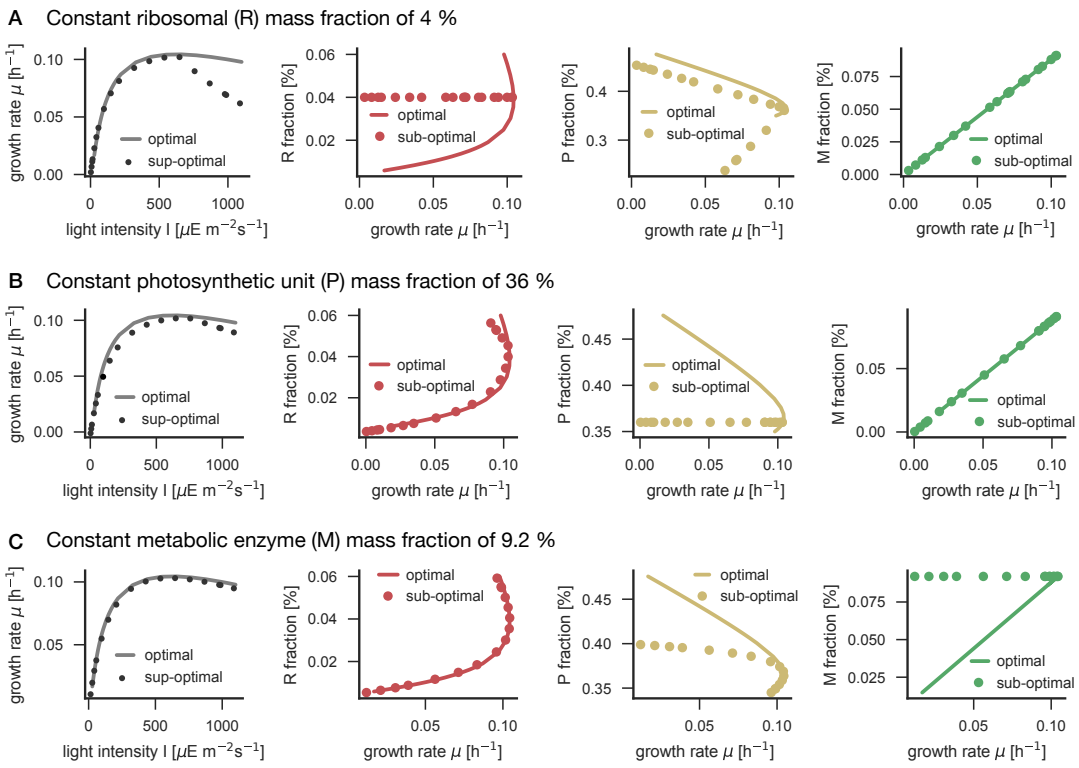

Figure 6–Figure supplement 2. Influence of constant enzyme fractions in the model on cellular growth rate.